

國立臺灣大學理學院化學系

碩士論文

Department of Chemistry

College of Science

National Taiwan University

Master Thesis



光系統 II 核心複合體能量傳遞動力學的理論研究
A Theoretical Study of Energy Transfer Dynamics in the
Photosystem II Core Complex

謝守庭

Shou-Ting Hsieh

指導教授：鄭原忠教授

Advisor: Yuan-Chung Cheng, Ph.D.

中華民國 107 年 7 月

July, 2018



國立臺灣大學碩士學位論文
口試委員會審定書

光系統 II 核心複合體能量傳遞動力學的理論研究
A Theoretical Study of Energy Transfer Dynamics in
the Photosystem II Core Complex

本論文係謝守庭君 (R05223127) 在國立臺灣大學化學系完成之碩士學位論文，於民國 107 年 7 月 24 日承下列考試委員審查通過及口試及格，特此證明

口試委員：

謝厚忠

朱修安

洪其輝

所長：

陳逸聰





摘要

光合作用是地球上生物生存裡非常重要的過程。它開始於光合收光複合體 (LHC)，收集太陽光並將能量傳給反應中心 (RCs)。作為氧氣生成引擎的光系統 II (PSII) 核心複合體是關鍵的光合作用複合體之一。PSII 核心複合體是一個對稱二聚體，它包含四個天線複合體 (CP43 和 CP47) 和兩個反應中心 (RC)。要了解這種複雜的光合作用複合體中的能量傳輸需要有效的理論模型，這樣的模型可以忠實地再現系統中的激發態能量轉移過程。在這項工作中，我們基於先前的分子動力學 (MD) 模擬研究結果提出了 PSII 核心複合體中激發態能量轉移的有效模型並根據 modified Redfield theory 計算激發態之間能量轉移的速率常數。它描述了 297 K 時 CP47、CP43 以及 RC 的吸收光譜以及 PSII 中 37 個發色團之間的全激發能量轉移動力學。此外，在我們的模型中，也考慮了兩種主要電荷分離途徑 P_{D1} 途徑和 Chl_{D1} 途徑。我們發現在 PSII 核心複合物的單體中，從 CP43 (CP47) 到 CP47 (CP43) 的激發態能傳遞過程最有可能通過 RC。此外，我們發現 CP47 有作為能量調節器的功能，它可以傳遞單體之間的激發態能量，並且當兩個 RC 中有一個在關閉的狀態時，使得 PSII 核心複合物保持高效率的電荷轉移。最後，我們發現 CLA625 可能是兩種 PSII 核心複合物單體之間能量傳遞的橋樑。我們的結果提出了 PSII 核心複合物構建成二聚體結構的可能原因。此外，也為理解 PSII 核心複合體中的光捕獲提供了新的見解，並且展示基於分子動力學模擬和量子化學計算的第一種原理方法可以有效地用於闡明複雜光合複合體中光捕獲的動力學。





Abstract

The Photosystem II (PSII) core complex, the engine for oxygen generation, is an important photosynthetic complex. It is a symmetric dimer that contains four antenna complexes (CP43 and CP47) and two reaction centers (RCs). Understanding energy transport in such complex photosynthetic complexes requires theoretical effective models that can faithfully reproduce excitation energy transfer (EET) dynamics. In this work, we present an effective model for EET in the PSII core complex based on a previous molecular dynamics (MD) simulation study. This model describes absorption spectra of CP47, CP43 and RC at 297 K as well as the full EET dynamics among the 74 chromophores in the PSII. Energy transfer rate constants are modeled based on the modified Redfield theory and two pathways of primary charge separation are treated phenomenologically in our model. We show that in the monomer, EET between two antenna complexes most likely occurs presumably through the RC. Also, the CLA625s are a bridge between monomers and cause the CP47s to become an energy regulator, which can transfer the excitation energy between monomers and maintain high efficiency of charge transfer when one of RCs is closed. CP47s as an energy regulator may be the reason for the dimeric structure of PSII core complex. Our model provides new insights towards the understanding of light harvesting in the PSII core complex and shows that a first principle approach based on MD simulations and quantum chemistry calculations can be effectively utilized to elucidate the dynamics of light harvesting in photosynthetic complexes.





Contents

口試委員會審定書	iii
摘要	v
Abstract	vii
1 Introduction	1
1.1 Light harvesting and charge transfer of oxygenic photosynthesis	1
1.1.1 The structure of photosystem II	2
1.1.2 Primary charge separation in the reaction center	5
1.1.3 Efficient EET and high quantum yield (QY) of charge transfer (CT)	6
1.1.4 Two models for energy and electron transfer in the PSII	7
1.2 What is the role of the dimeric PSII core complex?	9
1.3 The outline of this work	9
2 Theoretical background	13
2.1 Structure-based model for photosynthetic complexes	13
2.1.1 System-bath model and Frenkel exciton Hamiltonian	13
2.1.2 Methods for estimation of the site energy	16
2.1.3 Methods for estimation of the excitonic coupling	19
2.2 Quantum correction of classical time correlation function from MD	20
2.2.1 Classical time correlation function from MD	21

2.2.2	Harmonic quantum correction of energy gap auto-correlation function	23
2.3	Simulation of the absorption spectrum	24
3	Effective models for RC, CP47 and CP43	29
3.1	Model Hamiltonian	29
3.1.1	Pigment labels of PSII core complex	29
3.1.2	Block Hamiltonians of PSII core complex	30
3.2	An effective model for RC	34
3.2.1	Calibration of H_{RC}	34
3.2.2	Frenkel exciton Hamiltonian of RC	36
3.3	Effective models for CP47 and CP43	39
3.3.1	Calibration of H_{CP47} and H_{CP43}	39
3.3.2	Frenkel exciton Hamiltonian of CP47	40
3.3.3	Frenkel exciton Hamiltonian of CP43	42
4	Effective model for PSII core complex monomer (C1)	45
4.1	Master equation and rate constant matrix based on MRT	45
4.2	Exciton states and inter-complex excitonic couplings for PSII core complex monomer (C1)	47
4.3	Excitation energy transfer dynamics in a monomer of PSII core complex(C1)	50
5	An effective model for PSII core complex (C2)	53
5.1	Exciton states and inter-monomer excitonic couplings for PSII core complex (C2)	53
5.2	Excitation energy transfer dynamics in PSII core complex(C2)	55
5.3	Mutation and a closed RC for PSII core complex	57
5.3.1	Excitation energy transfer for PSII core complex without CLA625s	58
5.3.2	Excitation energy transfer for PSII core complex with a closed RC	61
5.3.3	Excitation energy transfer for mutant PSII core complex with a closed RC	63



6 Conclusion

65

Bibliography

67



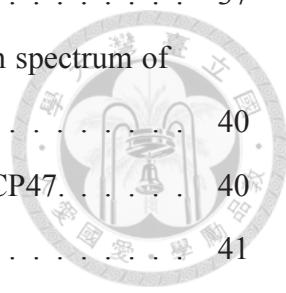




List of Figures

1.1	Illustration of light reaction in the PSII of higher plants.	2
1.2	A structural model of $C_2S_2M_2$ -type PSII-LHCII supercomplex.	3
1.3	The crystal structure of PSII core complex in <i>T. vulcanus</i> at a resolution of 1.9 Å.	4
1.4	Illustration of the chlorophyll arrangement in the PSII core complex.	5
1.5	Chromophores in the RC and oxygen-evolving complex (OEC).	6
2.1	The schematic diagram for CDC method.	17
2.2	Surface plot of the difference in electron density and the corresponding electronic potential for chlorophyll a.	18
2.3	Surface plot of transition density and the corresponding electrostatic potential for chlorophyll a.	19
2.4	The schematic diagram for TrEsp method.	20
2.5	The trajectories of site energy and excitonic coupling from MD.	21
2.6	One of the trajectories for energy-gap fluctuation of P_{D1}	22
2.7	The average energy gap auto-correlation function based on MD simulation.	23
2.8	The quantum time correlation function based on MD simulation.	25
3.1	Labels of 35 chlorophylls a and 2 pheophytins in the monomer of PSII core complex.	30
3.2	Block Hamiltonians in the system Hamiltonian.	31
3.3	The simulated absorption spectrum of the PSII RC based on raw MD data.	34
3.4	The simulated absorption spectrum of the PSII RC after the correction.	36
3.5	Average site energies of each pigments in the RC.	36

3.6	Excitonic couplings and exciton states in the RC.	37
3.7	(a) The absorption spectrum of the CP43 (b)The absorption spectrum of the CP47	40
3.8	Average site energies and positions of each pigment in the CP47.	40
3.9	Excitonic couplings and exciton states in the CP47.	41
3.10	Average site energies and positions of each pigment in the CP43.	43
3.11	Excitonic couplings and exciton states in the CP43.	44
4.1	Excitonic couplings of pigments between antenna complexes, CP47 and CP43, and a RC.	48
4.2	Exciton states in a monomer of PSII.	49
4.3	Excitation energy transfer with initial excitation at the CP47.	50
4.4	Excitation energy transfer with initial excitation at the CP43.	52
5.1	Exciton states in the PSII core complex.	54
5.2	Excitation energy transfer for PSII core complex with initial excitation at the CP47.	56
5.3	Excitation energy transfer for PSII core complex with initial excitation at the CP43.	57
5.4	Illustration of PSII core complex without CLA625s.	58
5.5	Excitation energy transfer for PSII core complex without CLA625s.	59
5.6	Illustration of CP47s as an energy regulator.	60
5.7	Excitation energy transfer for PSII core complex with a closed RC.	62
5.8	Excitation energy transfer for mutant PSII core complex with a closed RC.	63
5.9	Illustration of PSII core complex with β -carotenes.	64





List of Tables

3.1	The delocalization of exciton states in the RC	39
3.2	The delocalization of the RC	42
3.3	The delocalization of the RC	44





Chapter 1

Introduction

1.1 Light harvesting and charge transfer of oxygenic photosynthesis

Oxygenic photosynthesis is a type of photosynthesis that can produce oxygen. The oxidation of water to molecular oxygen is carried out by the oxygen-evolving complex (OEC) of photosystem II (PSII). This process requires absorption of multiple photons. PSII is a membrane-bound pigment-protein complex that captures sunlight and transfers light energy to the reaction center (RC) in order to generate a light-induced charge separation. The charge separation is initiated by a primary chlorophyll-*a* electron donor and forms a strong oxidant, $P680^+$. $P680^+$ promotes the formation of the oxygen, the proton and the electron which then is transferred from OEC to RC to reduce $P680^+$ and re-open the RC [1] [2]. The relationship between energy transfer and electron transfer is showed in Fig. 1.1.

Sunlight drives the primary charge separation in the RC. Therefore, how sunlight is collected and transferred efficiently to the RC is a key question to be understood. We will introduce the structure of PSII, primary charge separation in the RC, the high quantum yield of charge separation, and two models for energy transfer and charge transfer in the following subsections.

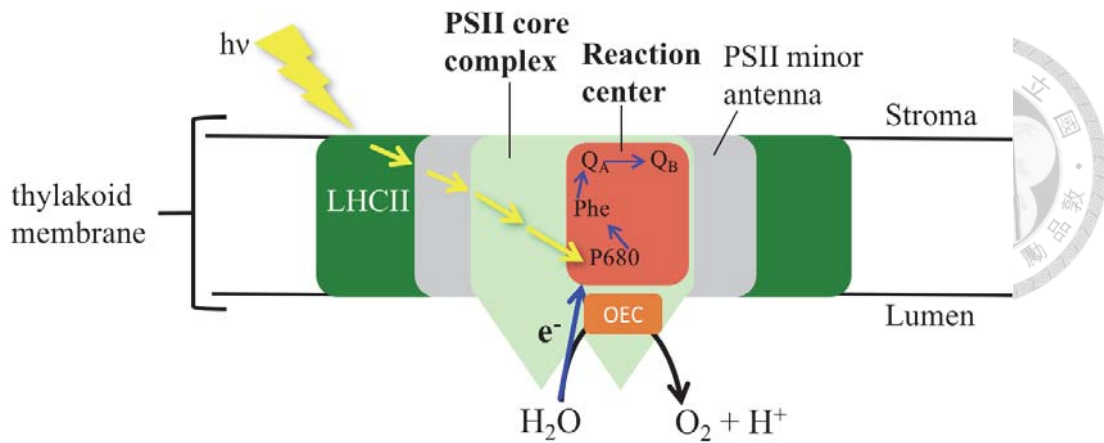


Figure 1.1: Illustration of light reaction in the PSII of higher plants. The PSII is located in the thylakoid membrane. Black lines indicate the thylakoid membrane. Yellow arrows indicate the light harvesting from peripheral light harvesting complex II (LHCII) to the reaction center (RC). Blue arrows indicate the path of electron transfer. Phe is the pheophytin. Q_A and Q_B are plastoquinones. OEC is the oxygen-evolving complex.

1.1.1 The structure of photosystem II

PSII is a complicated pigment-protein complex embedded within the thylakoid membrane of cyanobacteria, algae and higher plants. In green plants, the thylakoid membrane frequently form stacks of disks, and the continuous aqueous phase enclosed by the thylakoid membrane is the thylakoid lumen. The thylakoid lumen plays an important role for photophosphorylation during photosynthesis. In Fig. 1.1, the surface which the OEC attached to is the luminal surface and the other side is the stomal surface [3].

In plants, the PSII supercomplex contains a variety of peripheral light-harvesting complexes, including the major light-harvesting complexes II (LHCII), minor antenna complexes (CP29, CP26, and CP24). These antenna complexes surround the PSII core complex and absorb light energy and transmit it to the reaction center to promote charge separation [3, 4]. The structural model of PSII supercomplex is shown in Fig. 1.2.

The high-resolution crystal structure of PSII-LHCII supercomplex has been solved until 2016 [4]. To understand the pathways of excitation energy transfer, electron transport and water splitting processes occurring within the complex, the higher-resolution crystal structure of cyanobacterial PSII is applied in the previous studies [6, 3, 7, 8, 9]. The thylakoid membranes in cyanobacteria are different from that observed in plants. They form

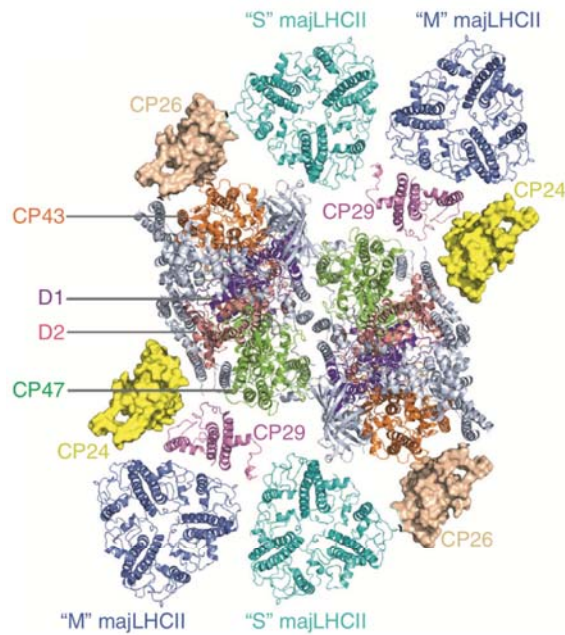


Figure 1.2: A structural model of $C_2S_2M_2$ -type PSII-LHCII supercomplex. The model was constructed based on the electron microscopy map and the crystal structures of PSII (PDB: 3ARC), majLHCII (PDB: 1RWT) and CP29 (PDB: 3PL9). Subunits D1, D2, CP43 and CP47 of PSII core are colored in purple, salmon red, orange and green, respectively. 'S' -, 'M' -type of majLHCII trimers and the minor antenna CP29 are shown as cyan, blue and magenta ribbons. The homologous structures of CP26 and CP24 are shown as wheat and yellow surface models, respectively [5].

stacks of parallel sheets close to the cytoplasmic membrane with a low packing density [10]. The relatively large distance between the thylakoids provides space for the external light- harvesting antenna in cyanobacteria, which is phycobilisomes rather than the LHCIIs in green plants [11]. However, based on the endosymbiotic theory, the cyanobacteria are the original of chloroplasts of algae and plants [1], so the PSII core complex of cyanobacteria is similar to that in plants [1, 12]. Except for the similar structure of PSII core complex, the mechanism of photosynthesis in cyanobacteria is similar to that in photosynthetic eukaryotes [2].

In 2014, Huang and co-workers reported an exciton model via extensive molecular dynamics (MD) simulations and quantum mechanics molecular mechanics calculations based on the X-ray structure of *Thermosynechococcus vulcanus* [13, 14]. Through collaboration, we obtain the MD simulation data. Therefore, our study is also based on the crystal structure of *T. vulcanus*.

The crystal structure of PSII core complex in *T. vulcanus* is showed in Fig. 1.3.

Figure 1.3 shows protein subunits and positions of pigments. According to positions of pigments showed in Fig. 1.3b, we can find that PSII core complex is a dimer with C2 symmetry.

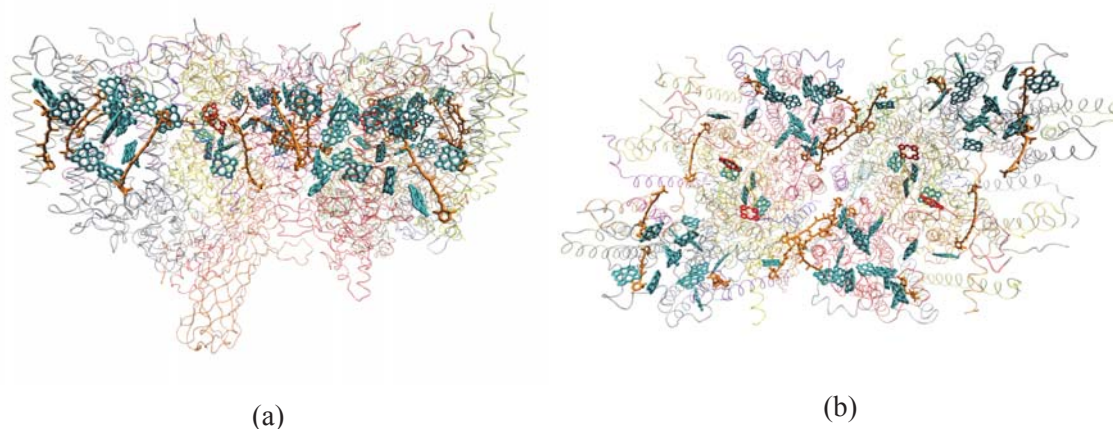


Figure 1.3: The crystal structure of PSII core complex in *T. vulcanus* at a resolution of 1.9 Å. (a) The side view of PSII core complex. (b) The top view of PSII core complex. The helical ribbons in the background are protein subunits. The chlorin ring of chlorophylls a and pheophytins are showed. The color code for chromophores are : CLA (cyan), PHE (red) and BCR (orange).

PSII core complex forms a C2 symmetric dimer. In each monomer, it includes two antenna complexes (CP43 and CP47) and one reaction center (RC). The location of antenna complexes and reaction centers are shown in Fig. 1.4. The blue, green, and red ellipses represent the location of CP47, CP43, and RC. Two CP47s in different monomers are nearest neighbors to each other, while two CP43s in different monomer are far away from each other. To understand light harvesting in the PSII core complex, our study focused on the chromophores in the PSII core complex. It includes 70 chlorophylls a (CLAs), 4 pheophytins (PHEs). In addition, there are 16 CLAs in a CP47, 13 CLAs in a CP43 and 6 CLAs and 2 PHEs in a RC. Therefore, there are 74 pigments considered in our model.

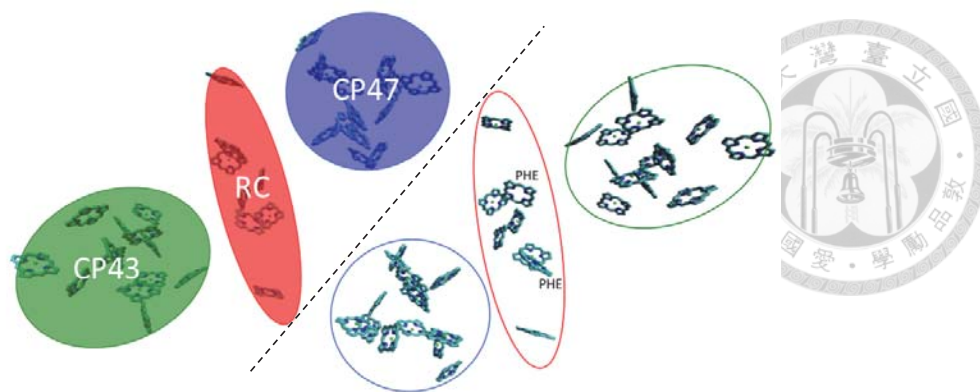
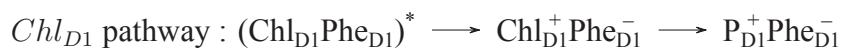


Figure 1.4: Illustration of the chlorophyll arrangement in the PSII core complex. Chlorin rings in the crystal structure of *T. vulcanus* PSII core complex (PDB: 3ARC) are shown. The blue ellipse represents the location of CP47 antenna complex. The red ellipse represents the location of RC. The green ellipse represents the location of CP43 antenna complex. Dashed lines indicate estimated interfacial regions between the two monomers.

1.1.2 Primary charge separation in the reaction center

The RC, the core of PSII, is the place where the primary charge separation takes place. There are 6 chlorophylls a, 2 pheophytins and 2 plastoquinones in a RC. In Fig. 1.5, chromophores in the RC form two symmetric branches. The closest two chlorophylls a, P_{D1} and P_{D2} , are named as a special pair. The distance between a special pair is only 8.06 Å. Therefore, a special pair is strongly coupled to each other.

An interesting phenomenon is that the primary charge separation only takes place in one branch. According to the previous studies [15, 16], there were two pathways to charge transfer in the RC, the so-called Chl_{D1} pathway and P_{D1} pathway [17]. The reactions are as follows:



In both pathways, they finally transfer an electron to pheophytin to form the same radical pair, $P_{D1}^+Phe_{D1}^-$. Then, the electron is transferred to Q_A and then transferred to the Q_B in order to leave the RC. Due to this functional asymmetry of two branches, the branch in which the electron transfer takes place is called the active chain and the other is called the inactive chain.

Because of the charge transfer dynamics in the RC are out of the range of our work,

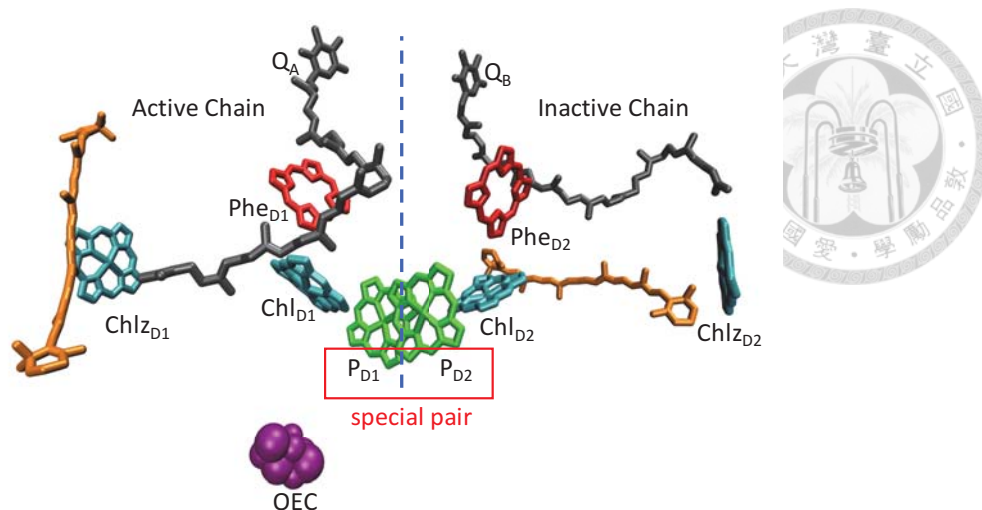
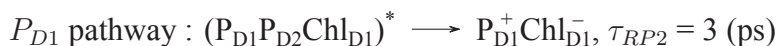
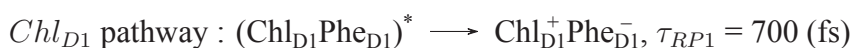


Figure 1.5: Chromophores in the RC and oxygen-evolving complex (OEC). The color code for chromophores are : CLA (cyan), PHE (red), BCR (orange), plastoquinone (gray) and OEC (purple).

we only consider two apparent time constants for formations of radical pair 1 (RP1), $Chl_{D1}^+ Phe_{D1}^-$, in Chl_{D1} pathway and radical pair 2 (RP2), $P_{D1}^+ Chl_{D1}^-$, in P_{D1} pathway:



in the master equation to mimic the charge transfer in the RC [16].

1.1.3 Efficient EET and high quantum yield (QY) of charge transfer (CT)

Another question that scientists are curious about is how efficient is energy conversion in the RC. If it is higher than the efficiency of current solar cell, then we would be possible to improve materials by understanding the reasons why the PSII can progress such efficient reaction. So, how can we measure the efficiency of primary charge separation? In previous studies [18, 19, 20, 21], time-resolved fluorescence is applied to measure the quantum efficiency of charge separation in PSII of a higher plant. Croce and his co-workers measured fluorescence decay traces with charge separation and without charge separation in the PSII at 680 nm. The quantum efficiency of charge separation is defined

by:

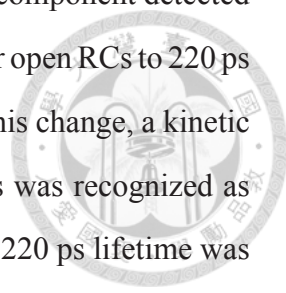
$$\Phi_{CS} = 1 - \frac{\tau_{avg}}{\tau_{Chl}}, \quad (1.1)$$

where τ_{avg} and τ_{Chl} are the average lifetime of an excited state in PSII in the present and absence of charge separation [19]. Pigments in the excited states can relax to the ground states by fluorescence, relaxation as heat or transferring energies to RCs to charge transfer. In other words, these three ways compete with each other. Fluorescence decay trace decays faster when the charge separation takes place in the PSII. Therefore, the ratio of average fluorescence lifetimes in the present and absence of charge separation implies the quantum efficiency of charge separation.

Croce and his co-workers prepare PSII samples with different peripheral antenna sizes. The results show that the quantum efficiency of charge separation in the PSII often exceeds 0.84, whereas in the PSII with smaller antenna size, the quantum efficiency can be as high as 0.91. Because excitation energies in large antenna take more time to reach a reaction center, some of them could be released by the fluorescence. Therefore, efficient excitation energy transfer from antenna complexes to a RC is a key factor that affect the efficiency of light reaction.

1.1.4 Two models for energy and electron transfer in the PSII

To understand the functional role of excitation energy transfer in PSII core complexes, it is necessary to consider the downstream electron transfer chain, too. The direction of excitation energy transfer in PSII core complexes not only transports from high-energy states to low-energy states but also toward RCs, which is driven by the depletion of the excitation population by charge separation. In the past few decades, the energy transfer and electron transfer in PSII cores were studied by a series of spectroscopic techniques such as linear spectra [22, 23, 24, 25], pump-probe [15], time-resolved fluorescence [23, 6], hole burning [26], and Stark spectroscopy [25]. The accumulated data have allowed a great deal of understanding on the light reaction in PSII, yet some key mechanisms regarding the relative time scales of energy transfer and charge separation remain controversial.



In the 1980s, Holzwarth and co-workers observed that the main component detected in the fluorescence decay of PSII core complexes change from 80 ps for open RCs to 220 ps for closed RCs, in which Q_A is in the reduced state [27]. To explain this change, a kinetic model was developed: the 80 ps lifetime component with open RCs was recognized as the contribution of primary electron transfer to a pheophytin, and the 220 ps lifetime was attributed to the secondary electron transfer to Q_A [28]. The kinetic model was called the "exciton radical pair equilibrium" (ERPE) model [27], because it proposed that the excitation energy transfer through the antenna to the RC is much faster than the overall charge separation time. As a result the equilibrium between excitation in the antenna and the charge separation state can be established. However, the crystal structure showed that the distance of antenna chlorophylls and RC chlorophylls is larger than 25 Å [13], and the distance is so far that energy transfer from antenna complexes to RCs should be slower than the overall charge separation in the RC. Therefore, the energy transfer to the RC should not be reversible. This leads to the so-called "transfer-to-the-trap limited" (TTTL) model [29].

Clearly, the relative time scales of energy transfer to be versus that of charge transfer distinguishes the ERPE model and the TTTL model. However, the reported time scales of energy transfer and charge transfer are inconsistent in the lifetime. It is due to the difficulty to assign a peak as the contribution of a specific site because the energy difference of transition energies in different sites are too close and sites strongly couple to each other. Also, radical pair (RP) formation and excitation energy transfer between chlorophylls both show spectral signatures in the Q_y region in PSII. These processes greatly complicates the interpretation of the transient absorption data. Therefore, it leads to an extensive debate in the literature regarding the mechanism and the timescale of energy transfer and charge transfer in PSII [22]. Until now, which one of the two kinetic models for energy and electron transfer is correct remain debate.

1.2 What is the role of the dimeric PSII core complex?

Up to now, we introduced the structure of dimeric PSII core complex, the high quantum yield of charge separation in RC and two kinetic model for energy and electron transfer in PSII core. It is worth noting that most studies did not consider an intact PSII core complex in the models. According to a previous study [30], there is no significant difference between the ground state absorption spectra of monomer and dimer. It implies that the interaction between the two monomers is weak. Therefore, a monomer of PSII core complex is often considered to describe light reaction in the PSII. However, if excitation energy can't flow between two monomers, why is the PSII in the form of dimer? What is the structure-function relation in PSII core complex? Recent experimental and theoretical studies [30, 31, 32] started to answer these questions. However, assumptions proposed by the studies still remain debate.

In addition, previous studies considered a simple model for PSII supercomplex to investigate energy transfer dynamics [33]. Van Amerongen and co-workers provided a coarse-grained model to correlate excitation energy transfer processes to the fluorescence kinetics of PSII. The coarse-grained model is based on dimeric structure of the PSII supercomplex. A hopping rate was applied in the model to evaluate the average migration time in the PSII. In their model, excitation energy can only transfer within different monomers by the CP47 and the RC in different monomers. However, the distance of the nearest pigments in two CP47 is 29.01 Å and is smaller than the distance of the nearest pigments of the CP47 and the RC in different monomers, which is 29.40 Å [13]. Therefore, the energy transfer link should be consider between two CP47s, too.

1.3 The outline of this work

In the previous study [14], Huang and co-workers performed five independent 5 ns molecular dynamics (MD) simulations based on the crystal structure of *T. vulcanus*. They calculated excitonic couplings and site energies for pigments in the PSII core complex based on structure ensembles from MD simulation. The effect of protein environment

was considered in the calculation of the average excitonic coupling and the average site energy obtained from MD simulation. According to their study, the site energy of Chl_{D1} was lowered by charged residues of the protein environment. It led Chl_{D1} to have the lowest site energy and excitation energy to flow to Chl_{D1} eventually. However, their study only considered static results and did not analyze the dynamics of results from MD simulation. Therefore, through collaboration, we obtain MD simulation data from Huang's group to analyze the dynamics simulated by MD. We aim to investigate the inter-monomeric excitation energy transfer pathway and want to know whether the dimeric structure of PSII core complex is crucial for excitation energy transfer based on the information obtained from MD simulation.

Based on the five independent simulation, they simulate another thirty 50 ps simulations. They saved a snapshot per 4 ps and save 12501 conformations of PSII core complex in each 50 ps simulations. They apply structure ensembles from MD to calculate the site energy for each pigments by CDC method. Therefore, we want to apply these *ab initio* data to construct an effective model of PSII core complex to try to understand the role of dimeric PSII core complex.

Average site energies obtained from CDC method and excitonic couplings based on crystal structure will be apply to construct the system Hamiltonian of the PSII core complex. Then, we will apply energy gap fluctuations for each site from MD simulation to calculate the energy gap auto-correlation function to describe the interaction between the environment and electronic states of pigments. After that, we will apply quantum correction to obtain the quantum time correlation function to ensure that the simulation of excitation energy transfer dynamics obeys detailed balance.

To verify the credibility of our model, we will fit absorption spectra of CP47, CP43 and RC, respectively. Then, we will revise our model until the model can describe absorption spectra well. And then, we will propagate the excitation energy transfer dynamics based on modified Redfield theory and master equation and will also consider two charge separation pathway and fluorescence in our simulation.

We expect that through the effective model constructed in this work, we can propose

an explanation for a reason why PSII core complex form into a dimeric structure in nature and propose a possible inter-monomeric excitation energy transfer pathway.







Chapter 2

Theoretical background

2.1 Structure-based model for photosynthetic complexes

In the past decades, to understand the energy transfer dynamics, the well-established model is developed. In the following sections, we will introduce the system-bath model to describe the pigment-protein complexes (PPCs) and the method to obtain transition energies and excitonic couplings.

2.1.1 System-bath model and Frenkel exciton Hamiltonian

The description of the quantum dynamics of excitons in pigment-protein complexes (PPCs) is well established [34, 35, 36, 37]. The standard Hamiltonian of a PPC used to study energy transfer contains three parts

$$H = H_s + H_b + H_{sb} \quad (2.1)$$

where H_s is the system Hamiltonian. H_b is the bath Hamiltonian and H_{sb} is the system-bath Hamiltonian [34].

The system Hamiltonian is the Frenkel exciton Hamiltonian. In the pigment-protein complex, the distance between most of the pigments is too large to have spatial overlap between the electronic wave functions of the different pigments, so the of Frenkel excitons

can be applied. [35] It is given by

$$H_s = \sum_n E_n |n\rangle \langle n| + \sum_{n \neq m} J_{nm} |n\rangle \langle m|, \quad (2.2)$$

where E_n is the transition energy of each sites and J_{nm} is the excitonic coupling for each pairs of sites. In our model, the localized excited state $|n\rangle$ is given as the product of the Q_y excited state (S_1) wavefunction $\psi_n^{(e)}(\mathbf{r})$ of pigment n and ground state wavefunctions $\psi_k^{(g)}(\mathbf{r})$ of pigment $k \neq n$, that is

$$|n\rangle = \psi_n^{(e)}(\mathbf{r}) \prod_{k \neq n} \psi_k^{(g)}(\mathbf{r}). \quad (2.3)$$

The excitonic coupling contains two parts. One is coulomb term and the other is exchange term. Exchange term is short-range contribution due to electron exchange. Coulomb term is the coulomb interaction between the electrons stay at their molecules. The Coulomb term which dominates the large majority of excitonic couplings between photosynthetic pigments, J_{nm} is given by

$$J_{nm} = \int dr_1 \dots dr_N \int d\bar{r}_1 \dots d\bar{r}_N \psi_n^{(e)}(r_1 \dots r_N) \psi_m^{(g)}(\bar{r}_1 \dots \bar{r}_N) \times \sum_{i,j} \frac{1}{|r_i - \bar{r}_j|} \psi_n^{(g)}(r_1 \dots r_N) \psi_m^{(e)}(\bar{r}_1 \dots \bar{r}_N). \quad (2.4)$$

By using Pauli's principle for the exchange of electrons and changing names of integration variables, the above matrix element can be written as

$$J_{nm} = N_m N_n \int dr_1 \dots dr_N \int d\bar{r}_1 \dots d\bar{r}_N \psi_n^{(e)}(r_1 \dots r_N) \psi_m^{(g)}(\bar{r}_1 \dots \bar{r}_N) \times \frac{1}{|r_1 - \bar{r}_1|} \psi_n^{(g)}(r_1 \dots r_N) \psi_m^{(e)}(\bar{r}_1 \dots \bar{r}_N). \quad (2.5)$$

$$= \iint dr_1 dr_2 \rho_n(r_1) \frac{1}{r_1 - r_2} \rho_m(r_2),$$

$$\rho_n(r_1) = N_n \int dr_2 \dots dr_N \psi_n^{(e)}(r_1 \dots r_N) \psi_n^{(g)}(r_1 \dots r_N), \quad (2.6)$$

where $\rho_n(r_1)$ is the transition density of the pigment n [38].

The bath Hamiltonian is given as

$$H_b = \sum_{\alpha} \hbar\omega_{\alpha} (b_{\alpha}^{\dagger} b_{\alpha} + \frac{1}{2}), \quad (2.7)$$

where $\hbar\omega_{\alpha}$ is the energy of vibrational quanta in the mode α . Actually, it is hard to describe the environment exactly, so we apply a bunch of effective harmonic oscillators to approximate the motions from the bath. Here, we only consider the diagonal term of system-bath Hamiltonian and assume the off-diagonal term is zero. To verify that the assumption is reasonable or not, we calculate the ratio of standard deviations to absolute value of couplings, $\frac{\sigma}{|J|}$. This ratio implies the degree of excitonic coupling fluctuation. We only calculate the ratio of excitonic coupling which is larger than 10 cm^{-1} , because the excitonic coupling, which is smaller than 10 cm^{-1} , may result in a fake degree of fluctuation. We find that most of the ratio are less than 0.2. It means that pigments bound by proteins can rotate and vibrate in a limited space and leads to slight fluctuations of couplings between pigments. Therefore, ignoring the off-diagonal term of H_{sb} is reasonable and we just consider excitonic couplings as constant values in the system Hamiltonian.

The system-bath Hamiltonian is denoted by

$$H_{sb} = \sum_{\alpha} \sum_n \hbar\omega_{\alpha} g_{\alpha,n} (b_{\alpha}^{\dagger} + b_{\alpha}) |n\rangle \langle n| \quad (2.8)$$

where $g_{\alpha,n}$ is the system-bath coupling constant between the state n in the system and the mode α of the bath. The vibronic coupling of each element in the system-bath Hamiltonian describe the modulation of site energies and excitonic couplings by nuclear motions of the complex. It is assumed that the fluctuations of site energies are linear coupled to the displacements of nuclei from its equilibrium positions and each site has its own independent bath.

In condensed phased system, the number of vibrational modes coupled to sites is so large. Therefore, we apply the spectral density function, $J(\omega)$, to describe such interaction. Based on the independent bath assumption, the spectral density function for the site n is

defined as

$$J_n(\omega) = \sum_{\alpha} g_{\alpha,n}^2 \hbar^2 \omega_{\alpha}^2 \delta(\omega - \omega_{\alpha}). \quad (2.9)$$

The spectral density function is the density of state of vibration modes weighted by the effective interaction strength. In addition, in the energy gap Hamiltonian (Eq. 2.1-2.8), the energy gap fluctuation governs the quantum dynamics, which is described by the energy gap auto-correlation function, $C_n(\tau)$. It is given by:

$$\begin{aligned} C_n(\tau) &= \langle \delta E_n(\tau) \delta E_n(0) \rangle \\ &= \sum_{\alpha} g_{\alpha,n}^2 \hbar^2 \omega_{\alpha}^2 [\cos(\omega_{\alpha}\tau) \coth\left(\frac{\beta \hbar \omega_{\alpha}}{2}\right) - i \sin(\omega_{\alpha}\tau)] \\ &= \int_0^{\infty} d\omega J_n(\omega) [\cos(\omega\tau) \coth\left(\frac{\beta \hbar \omega}{2}\right) - i \sin(\omega\tau)], \end{aligned} \quad (2.10)$$

where $\beta = \frac{1}{k_b T}$ and T is the temperature of the thermal bath. Both the energy gap auto-correlation function and the spectral density function can estimate the interaction between the system and the bath. In our work, we calculate the time correlation function to describe system-bath interaction instead of the spectral density function.

2.1.2 Methods for estimation of the site energy

As we mentioned before, the matrix elements of system Hamiltonian are site energies and excitonic coupling. As long as we can obtain these matrix elements, we can determine a system Hamiltonian. The following subsection will introduce two methods of site energy calculation.

One of the methods is a calculation of site energies from a fit of optical spectra. N sets of site energies are generated, and the corresponding linear spectra such as OD, LD, and CD are simulated and compared to the experimental results. Then, the different sets are rank according to their fitness value, which is defined by the reciprocal of the mean square deviation between the calculated and experimental spectrum. Finally, we can obtain a set of site energies with the largest fitness value [39].

The other way to obtain a set of site energies is based on structural data of sites. Charge density coupling (CDC) method [39, 40] is one of the methods based on structural

data and is applied to calculate site energies based on MD trajectories from Huang's group. In this approach, the relative site energy is calculated rather than the absolute site energy. Figure 2.1 shows the idea of CDC method.

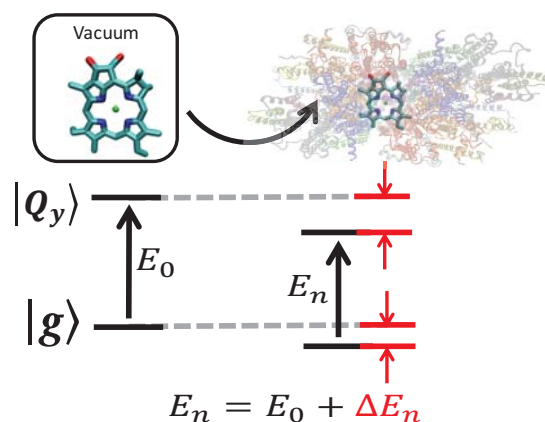


Figure 2.1: The schematic diagram for CDC method. The ground state and first excited state of Q_y transition are represented by bra-ket notation. Chlorin ring of chlorophyll a is shown. The helical ribbons in the background are protein subunits and represent the bath.

Vacuum transition energy, E_0 , is the energy shift obtained by fitting the spectrum and is assumed to be equal for all pigments. That is, we ignore the energy difference due to the conformation change. However, E_0 is changed by local protein environments of each sites and lead to different transition energies. Therefore, the site energy of pigment n is given by

$$E_n = E_0 + \Delta E_n \quad (2.11)$$

where ΔE_n is the site energy shift due to the difference in pigment-protein Coulomb interaction between the ground and excited states of the pigments. To simplify the calculation of Coulomb interaction between pigments and protein residues, Charge protein residues are considered as background charges, $\{q_j^{bg}\}$, and an electronic state of a pigment are represented by a set of atomic partial charge, $\{q_i\}$. Atomic partial charge is a charge localized on an atom of a pigment. A set of atomic partial charges is obtained from fitting of *ab initio* electronic potential. That is, the electronic potential of an electronic density approximate

the electronic potential of atomic partial charges. Thus, ΔE_n is given by:

$$\begin{aligned}\Delta E_n &= \frac{1}{\epsilon_{eff}} \sum_i \sum_j \left(\frac{q_{e,i}^n q_j^{bg}}{|r_i^n - r_j^{bg}|} - \frac{q_{g,i}^n q_j^{bg}}{|r_i^n - r_j^{bg}|} \right) \\ &= \frac{1}{\epsilon_{eff}} \sum_i \sum_j \frac{\Delta q_i^n q_j^{bg}}{|r_i^n - r_j^{bg}|},\end{aligned}\tag{2.12}$$



where ϵ_{eff} is an effective dielectric constant, $q_{e,i}^n$ is a atomic partial charge on atom i for the excited state of pigment n , $q_{g,i}^n$ is a atomic partial charge on atom i for the ground state of pigment n , Δq_i^n is the difference of a atomic partial charge on atom i for pigment n , and r_i^n or r_j^{bg} is the position of atomic partial charges or background charges. Figure 2.2 shows the difference of ground and excited electronic density of chlorophyll a and the difference of ground and excited electronic potential of chlorophyll a.



Figure 2.2: Surface plot of the difference in electron density and the corresponding electronic potential for chlorophyll a. (a) Surface plot of the difference in electron density $\Delta\rho(r) = \rho_e(r) - \rho_g(r)$ between the excited state, S_1 , and the ground state, S_0 obtained by TDDFT/B3LYP. (b) The corresponding electronic potential $\Delta\phi(r) = \phi_e(r) - \phi_g(r)$. Negative values are represented by red colors and positive values by blue colors [41].

2.1.3 Methods for estimation of the excitonic coupling

In the subsection 2.1.1, we mentioned excitonic coupling, J_{nm} . In the following subsection, we will present two methods to calculate excitonic coupling. As far as we know, excitonic coupling is given as:

$$J_{nm} = \iint dr_1 dr_2 \rho_n(r_1) \frac{1}{r_{12}} \rho_m(r_2). \quad (2.13)$$

In the transition density cube (TDC) method [42], transition density, $\rho(r)$, is represent as a set of three dimensional grids. According to Eq. 2.14, excitonic coupling is the integral with respect to r_1 and r_2 of accurate interaction energies between transition density cubes of each pigments. However, this method is evaluated numerically. Therefore, Transition charge from electrostatic potential (TrEsp) method, which is equal accuracy, but less numerical cost, is developed.

Figure 2.3 shows the transition density of chlorophyll a and the corresponding electrostatic potential of the transition density. In the TrEsp method [41], the electrostatic

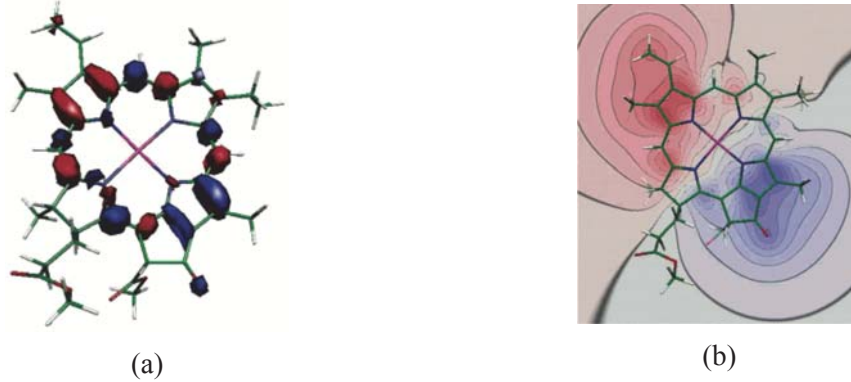


Figure 2.3: Surface plot of transition density and the corresponding electrostatic potential for chlorophyll a. (a) Surface plot of the transition density $\rho^T(r)$ of chlorophyll a obtained by TDDFT/B3LYP. (b) The corresponding electronic potential $\phi^T(r)$. Negative values are represented by red colors and positive values by blue colors [41].

potential of the transition density is fitting by transition charges which localize on atoms of a pigment. Thus, the excitonic coupling is given as:

$$J_{nm} = f \sum_i \sum_j \frac{q_i^{n,T} q_j^{m,T}}{|R_i^n - R_j^m|}, f = 2.68 \exp\{-0.27d\} + 0.54, \quad (2.14)$$

where f is a scaling factor to describe screening and polarization effect of the protein environment in an implicit way [43, 44], $q_i^{n,T}$ is the transition charge i of pigment n , $q_j^{m,T}$ is the transition charge j of pigment m , R_i^n is the position of transition charge i of pigment n , R_j^m is the position of transition charge j of pigment m , and d is the distance between pigment n and m . The schematic diagram for TrEsp method is showed bellow.

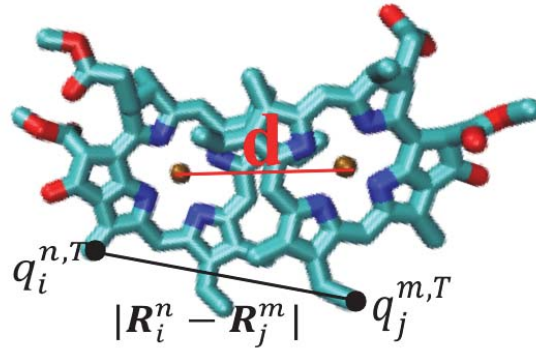


Figure 2.4: The schematic diagram for TrEsp method.

2.2 Quantum correction of classical time correlation function from MD

As we mentioned before, raw data of molecular dynamics (MD) simulation propagated by huang's group are structure ensembles of PSII core complex. We can calculate site energies and excitonic couplings by CDC method and TrEsp method based on structure ensembles from MD and have trajectories of site energies and trajectories of excitonic couplings. Figure 2.5 shows trajectories of site energy for P_{D1} and excitonic coupling between special pair, P_{D1} and P_{D2} .

In this section, we describe the interaction between our system and bath by the energy gap auto-correlation function (Eq. 2.10) from MD trajectories and obtain quantum time correlation function (qTCF) by quantum correction.

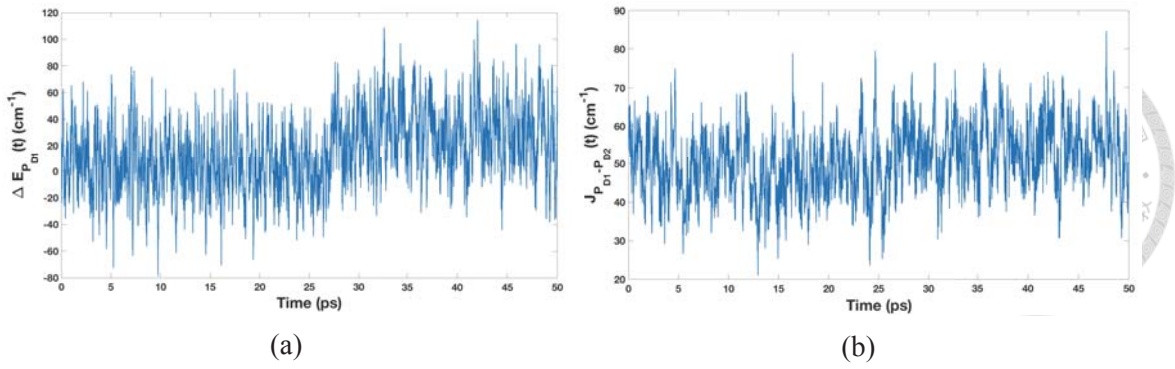


Figure 2.5: The trajectories of site energy and excitonic coupling from MD. (a) The trajectory of site energy obtain by CDC method for P_{D1} . X axis is the simulation time of MD. Y axis is the energy gap of site energy and unit is cm^{-1} . (b) The trajectory of excitonic coupling, J , obtain by TrEsp method between special pair. X axis is the simulation time of MD. The unit of Y axis is cm^{-1} .

2.2.1 Classical time correlation function from MD

As we mentioned before, we apply energy gap auto-correlation function to describe the interaction of the system and the bath. To obtain energy gap auto-correlation function, we need to have the trajectory of energy-gap fluctuation. For each pigments, we have six trajectories of site energy, $\Delta E_n(t)$. Then, the average value, $\overline{\Delta E_n}$, of site energy for all trajectories is applied in the diagonal term of system Hamiltonian. In addition, we can obtain energy gap fluctuation, $\delta E_n(t)$, for each pigments. The energy gap fluctuation is given by:

$$\delta E_n(t) = \Delta E_n(t) - \overline{\Delta E_n}. \quad (2.15)$$

For example, Fig. 2.6 shows one of the trajectories of energy gap fluctuation of P_{D1} . Energy gap fluctuation affect by the bath, such as vibration modes of pigments, vibration modes of proteins, slow conformational change of proteins. According to the previous literature, fast vibration modes of pigments and vibration modes of proteins contribute to the so-called dynamic disorder for energy gap fluctuation and slow conformational change of proteins contributes to the so-called static disorder. Protein conformational changes are on ms time scale. This time scale is larger than the ps time scale of energy transfer. Therefore, to investigation energy transfer dynamics, we only need to consider the dynamics disorder. In Fig. 2.6, we can find that site energy shifts around 27 ps. It may be due to protein conformational change. That is to say, the static disorder and the dynamics disorder.

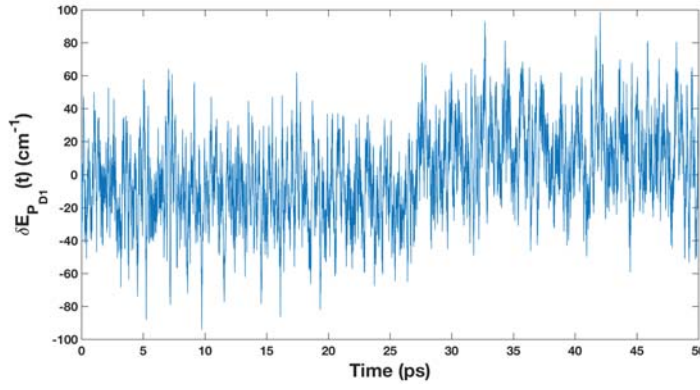


Figure 2.6: One of the trajectories for energy-gap fluctuation of P_{D1} . X axis is the simulation time of MD. Y axis is the energy-gap fluctuation of site energy and unit is cm^{-1} .

der of energy gap fluctuation are mixing in the trajectory. Therefore, we try to "filter" the static disorder by dividing the 50 ps trajectory to five intervals. Each interval is 10 ps and dominates by the dynamic disorder.

Then, we can calculate energy gap auto-correlation function based on 10 ps trajectories of energy gap fluctuation for each pigment. The energy gap time correlation function is given as:

$$C_n(\tau) = \langle \delta E_n(\tau) \delta E_n(0) \rangle. \quad (2.16)$$

According to ergodic theory, as long as measurements are performed over a long time, and that due to the flow of the system through state space, the time average is the the same as the ensemble average [45]. Therefore, we can rewrite the time correlation function (TCF) as time average and it is given as:

$$C_n(\tau) = \frac{1}{T} \int_0^T \delta E_n(\tau + t) \delta E_n(t) dt. \quad (2.17)$$

Each pigment has 30 trajectories for 10 ps and has corresponding 30 energy gap auto-correlation functions. We average 30 energy gap auto-correlation functions and each pigment has one average energy gap auto-correlation functions. Moreover, we assume pigments are coupled to independent baths of the same form. Therefore, we average energy gap auto-correlation functions of each pigment in the RC and this TCF is denoted as

C_{MD}^{avg} . It is given as:

$$C_{MD}^{avg}(\tau) = \frac{1}{30 \times 8 \times 2} \sum_{n=1}^8 \sum_{i=1}^{30} \sum_{j=1}^2 C_{n,i,j}(\tau), \quad (2.18)$$

where i is the index of 30 trajectories of energy gap fluctuation for each pigment and j is the index for monomer 1 (M1) or monomer 2 (M2). Figure 2.7 shows the average energy gap auto-correlation function from pigments.

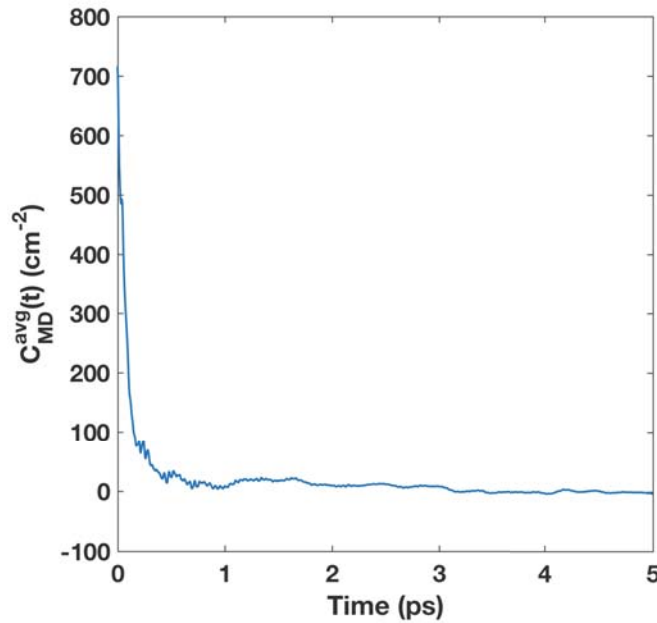


Figure 2.7: The average energy gap auto-time correlation function based on MD simulation. The unit of x axis is ps. The unit of y axis is cm^{-2} .

2.2.2 Harmonic quantum correction of energy gap auto-correlation function

To correctly simulate excitation energy transfer dynamics, the behavior of our model system has to obey detailed balance. As far as we know, quantum time correlation function (qTCF) describe the quantum dynamics of a system and also obey detailed balance. Quantum time correlation function is complex. It can't be directly measured but observables are often related to the real or imaginary part of correlation function. In our work, energy gap auto-correlation function, also known as classical time correlation function (cTCF), obtained by site energy fluctuation from MD simulation relates to the real part

of quantum time correlation function. Therefore, we need to apply quantum correction to cTCF to obtain qTCF.

We apply harmonic quantum correction to cTCF obtained by MD. Harmonic quantum correction corrects the cTCF in the frequency domain, so we apply the Fourier transform to cTCF to obtain classical time correlation function in frequency domain [46]. The classical time correlation function in frequency domain is given as:

$$C_{MD}^{avg}(\omega) = \int_{-\infty}^{\infty} e^{i\omega\tau} C_{MD}^{avg}(\tau) d\tau, \quad (2.19)$$

where ω is the angular frequency. We apply the Hann window to $C_{MD}^{avg}(\omega)$ to filter out the higher frequency modes. Then, $C_{MD}^{avg}(\omega)$ is multiplied by a harmonic quantum correction factor, $Q_{har}(\omega)$, to obtain quantum time correlation function in frequency domain. Harmonic quantum correction is given as:

$$C_{qc}(\omega) = Q_{har}(\omega) C_{MD}^{avg}(\omega) = \frac{\beta\hbar\omega}{1 - e^{\beta\hbar\omega}} C_{MD}^{avg}(\omega), \quad (2.20)$$

where $\beta = \frac{1}{k_b T}$ and T is the temperature. Then, $C_{qc}(\omega)$ is applied by inverse Fourier transform to obtain quantum time correlation function in time domain, $C_{qc}(\tau)$. The quantum time correlation function (qTCF) is complex. Figure 2.8 shows the qTCF. Real part intensity of qTCF at t=0 is higher than cTCF and the amplitude of fluctuation is higher than cTCF. It is due to the harmonic quantum correction factor emphasize the effective interaction strength of high frequency vibration modes. Imaginary part of qTCF fluctuates intensely within 2 ps. It may be due to high frequency vibration modes, too.

2.3 Simulation of the absorption spectrum

So far, we describe our model in the site basis. However, when the PSII core complex absorbs sunlight, there may be more than one pigment present in the excited state. Therefore, we diagonalize the system Hamiltonian in site basis to obtain the exciton state. The exciton state is eigenstate of system Hamiltonian and is superposition of all sites for

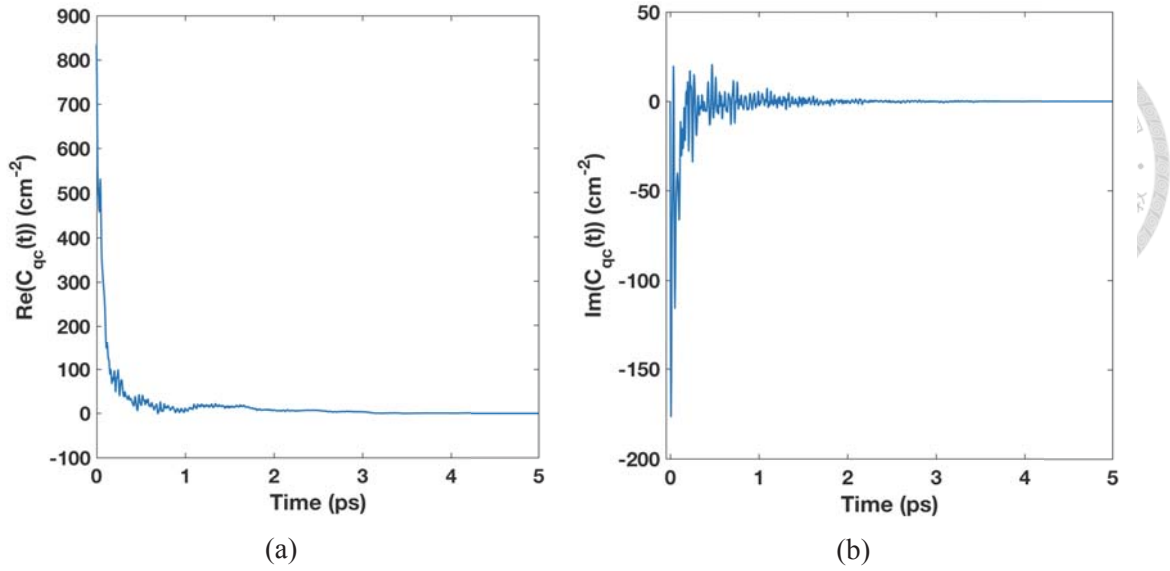


Figure 2.8: The quantum time correlation function based on MD simulation. (a) The Real part of quantum time correlation function. (b) The imaginary part of quantum time correlation function. The unit of x axis is ps. The unit of y axis is cm^{-2} .

PSII core complex. The exciton state, $|\alpha\rangle$, denote as:

$$H_s |\alpha\rangle = E_\alpha |\alpha\rangle, |\alpha\rangle = \sum_n C_n^\alpha |n\rangle. \quad (2.21)$$

where E_α is the exciton energy for the exciton state α , C_n^α is the coefficient for the site n in the exciton state α . Then, we can describe the absorption spectrum by exciton states and propagate excitation energy transfer dynamics by calculating the transfer rate between exciton states.

In the section 2.1, we introduce the structure-based model and methods to calculate site energies and excitonic couplings. In addition, in the previous section of chapter 2, we introduce the harmonic quantum correction to obtain the quantum time correlation function from energy gap auto-correlation function based on MD simulation. Then, we can construct an effective model for PSII core complex to investigate excitation energy transfer dynamics. However, how can we trust the dynamics given by our model? We verify our model by fitting the absorption spectra. If our model can reflect the spectral properties, we have confidence in our model. We apply optical density (OD) to simulate

the absorption spectrum [47, 37]. The optical density is given as:

$$OD(\omega) = \omega \sum_{\alpha} \mu_{\alpha}^2 Re \int_0^{\infty} dt e^{i(\omega - \omega_{\alpha})t - g_{\alpha\alpha\alpha}(t) - R_{\alpha\alpha\alpha}t}; \quad (2.22)$$

$$\mu_{\alpha} = \sum_n C_n^{\alpha} \mu_n; \quad (2.23)$$

$$R_{\alpha\alpha\alpha} = - \sum_{\beta \neq \alpha} R_{\beta\beta\alpha}, \quad (2.24)$$



where μ_{α} and ω_{α} denote the transition dipole moment and frequency of the α -th exciton state, $g_{\alpha\alpha\alpha}(t)$ is the line-broadening function, $R_{\alpha\alpha\alpha}$ is the inverse lifetime of the α -th exciton state. The coefficient, C_n^{α} , for the site n in the exciton state α associates the transition dipole of the exciton state with the molecular transition dipole, μ_n . It is important to note that the optical density takes into account a relaxation-induced broadening of the exciton states given by their inverse lifetimes, i.e., $R_{\alpha\alpha\alpha}$. $R_{\alpha\alpha\alpha}$ is given by a sum of the relaxation rates from the α -th exciton state to the others exciton states. $R_{\beta\beta\alpha}$ is the transition rate based on modified Redfield theory from α -th exciton state to β -th exciton state and is given by [47]:

$$R_{\beta\beta\alpha} = -2Re \int_0^{\infty} dt \hat{W}(\omega_{\beta\alpha}, t) \{ \dot{g}_{\beta\alpha\alpha}(t) - \{ \dot{g}_{\alpha\beta\alpha}(t) - \dot{g}_{\alpha\beta\beta}(t) + 2i\lambda_{\alpha\beta\alpha} \} \times \{ \dot{g}_{\alpha\alpha\beta}(t) - \dot{g}_{\beta\beta\alpha}(t) + 2i\lambda_{\alpha\alpha\beta} \} \}; \quad (2.25)$$

$$\hat{W}(\omega_{\beta\alpha}, t) = \exp\{-i\omega_{\beta-\alpha}t - g_{\alpha\alpha\alpha}(t) - g_{\beta\beta\beta}(t) + 2g_{\alpha\alpha\beta} + 2i(\lambda_{\alpha\beta\beta} - \lambda_{\alpha\alpha\alpha})t\} \quad (2.26)$$

where $\omega_{\beta\alpha} = \omega_{\beta} - \omega_{\alpha}$, $\lambda_{\alpha\alpha\alpha}$ is the reorganization energy for α -th exciton state. The lineshape function $g(t)$ and λ -value in Eq. 2.25 and 2.26 defined as

$$g_{\alpha\beta\gamma\delta}(t) = \int_0^t d\tau C_{\alpha\beta\gamma\delta}(\tau)(t - \tau) \quad (2.27)$$

$$\lambda_{\alpha\beta\gamma\delta} = - \int_0^{\infty} \text{Im}(C_{\alpha\beta\gamma\delta}(\tau)) d\tau \quad (2.28)$$

$$C_{\alpha\beta\gamma\delta}(\tau) = \int_0^{\infty} d\omega J_{\alpha\beta\gamma\delta}(\omega) [\cos(\omega\tau) \coth(\frac{\beta\hbar\omega\alpha}{2}) - i \sin(\omega\tau)], \quad (2.29)$$

where $J_{\alpha\beta\gamma\delta}(\omega)$ is the matrix of the spectral densities in the eigenstate (exciton) representation and can be obtained from the matrix of the spectral densities in the site representation $J_{nmn'm'}(\omega)$. We further assume that the spectral density of each such bath is site independent. That is, $J_{nmn'm'}(\omega) = \delta_{nm}\delta_{nn'}\delta_{mm'}J(\omega)$. Therefore, transformation to the eigenstate representation yields:

$$J_{\alpha\beta\gamma\delta}(\omega) = \sum_n C_n^\alpha C_n^\beta C_n^\gamma C_n^\delta J(\omega) \quad (2.30)$$

Therefore, energy gap auto-correlation function in exciton representation, $C_{\alpha\beta\gamma\delta}(\tau)$, can also be obtain from the site representation. It is given by:

$$\begin{aligned} C_{\alpha\beta\gamma\delta}(\tau) &= \sum_n C_n^\alpha C_n^\beta C_n^\gamma C_n^\delta \int_0^{\infty} d\omega J(\omega) [\cos(\omega\tau) \coth(\frac{\beta\hbar\omega\alpha}{2}) - i \sin(\omega\tau)] \\ &= \sum_n C_n^\alpha C_n^\beta C_n^\gamma C_n^\delta C(\tau), \end{aligned} \quad (2.31)$$

where $C(\tau)$ is energy gap auto-correlation function in site representation and we assume $C(\tau)$ is equal to $C_{qc}(\tau)$ obtained by $C_{MD}^{avg}(\tau)$. That is to say, we can calculate the Eq. 2.22 based on the $C_{qc}(\tau)$ and exciton energies and coefficients of exciton states.

However, we have to consider the homogeneous broadening and inhomogeneous broadening, which are due to the dynamic disorder and the static disorder of energy gap fluctuation, when we simulate the absorption spectrum. Since the simulation time of each MD trajectories is only 50 ps, the inhomogeneous broadening obtained by MD is biased, we set the inhomogeneous broadening as 70 cm^{-1} for all exciton states. The homogeneous broadening for the peak of the α^{th} exciton state is represented by the absorption line shape function of the α^{th} exciton state, $g_{\alpha\alpha\alpha\alpha}(t)$.

Furthermore, After verifying our model by fitting absorption spectrum, we can propa-

gate excitation energy transfer dynamics by construct the rate constant matrix. The matrix element of rate constant matrix can be obtained by Eq. 2.25. The details will be mentioned in section 4.1.





Chapter 3

Effective models for RC, CP47 and CP43

3.1 Model Hamiltonian

In this chapter, we present the effective model in our work based on site energies calculated by Huang's group and excitonic couplings calculated by ourselves based on crystal structure (PDB ID:3ARC). In following subsections, we present pigments labels for 74 chromophores in the PSII core complex to introduce matrix elements of system Hamiltonian. The system Hamiltonian is 74 by 74 matrix, so the system Hamiltonian is divided into 20 block Hamiltonians to discuss individually.

3.1.1 Pigment labels of PSII core complex

In the introduction, we show the crystal structure of PSII core complex, but we don't assign all the pigment labels to each pigments. However, the diagonal term of system Hamiltonian is site energy of each pigment. Therefore, we present pigments considered in our model in Fig. 3.1. The label of pigments are shown below.

In Fig. 3.1, we only show the monomer of PSII core complex, because the label are the same in two monomers. There are 16 chlorophylls a in the CP47 and these pigments are labeled from CLA612 to CLA627. There are 13 chlorophylls a in the CP43 and these

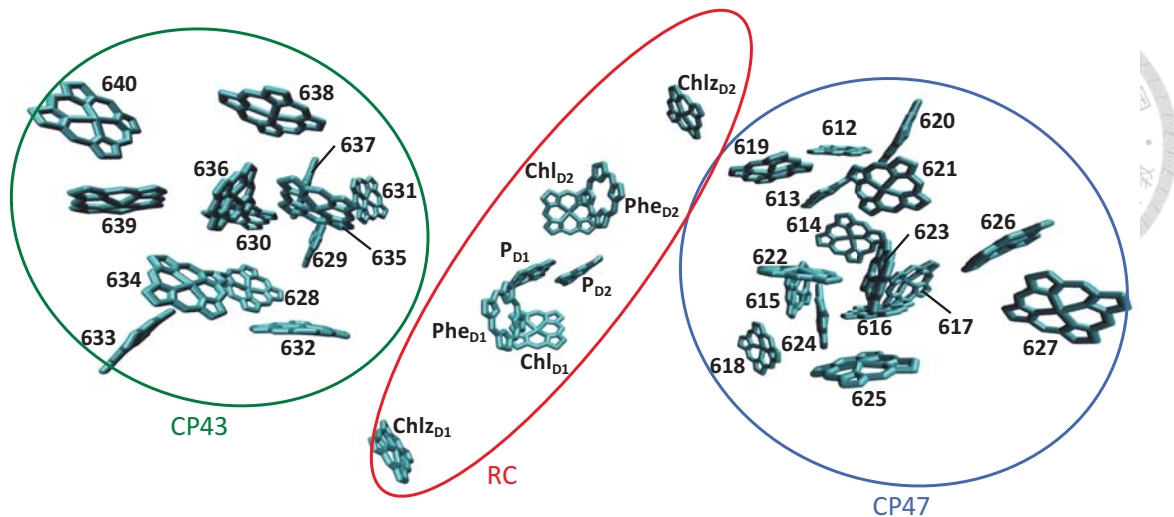


Figure 3.1: Labels of 35 chlorophylls a and 2 pheophytins in the monomer of PSII core complex. Chlorin rings in the crystal structure are shown. The blue ellipse represents the location of CP47 antenna complex and chlorophylls in the blue ellipse are in CP47 antenna complex. The red ellipse represents the location of RC. The green ellipse represents the location of CP43 antenna complex.

pigments are labeled from CLA628 to CLA640. In the RC, there are 6 chlorophylls a and 2 pheophytins. The subscripts, D1 and D2, represent two major proteins in the RC. Chl_{D1} and Chl_{D2} are also known as accessory chlorophylls. $Chlz_{D1}$ and $Chlz_{D2}$ are also known as peripheral chlorophylls.

3.1.2 Block Hamiltonians of PSII core complex

To clearly understand and analyze matrix elements of our system Hamiltonian, we divide the system Hamiltonian into 20 block Hamiltonians. There are 74 pigments in the PSII core complex, 37 pigments are in each monomers. $n=1-37$ represent pigments in M1 and $n=38-74$ represent pigments in M2. Site energies, E_n , are calculate based on MD simulation by huang's group and excitonic couplings, J_{nm} , are calculate based on crystal structure by ourself. Figure 3.2 shows block Hamiltonians in the system Hamiltonian.

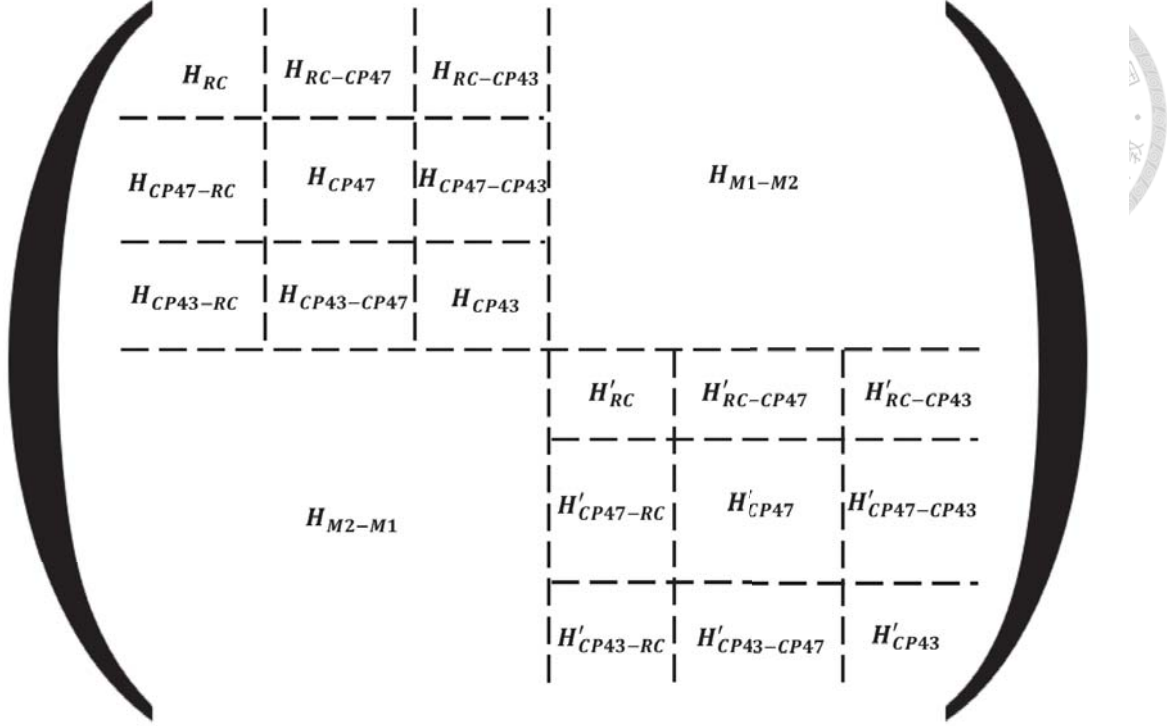


Figure 3.2: Block Hamiltonians in the system Hamiltonian. The whole matrix is a 74 by 74 system Hamiltonian. The name of each block Hamiltonian is shown in the center of the block. H_{RC} and H'_{RC} are 8 by 8 matrixes. H_{CP47} and H'_{CP47} are 16 by 16 matrixes. H_{CP43} and H'_{CP43} are 13 by 13 matrixes. $H_{CP47-RC}$ and $H'_{CP47-RC}$ are 16 by 8 matrixes. $H_{CP43-RC}$ and $H'_{CP43-RC}$ are 13 by 8 matrixes. $H_{CP43-CP47}$ and $H'_{CP43-CP47}$ are 13 by 16 matrixes. $H_{RC-CP47}$ is the transpose of $H_{CP47-RC}$. $H_{RC-CP43}$ is the transpose of $H_{CP43-RC}$. $H_{CP47-CP43}$ is the transpose of $H_{CP43-CP47}$. $H'_{RC-CP47}$ is the transpose of $H'_{CP47-RC}$. $H'_{RC-CP43}$ is the transpose of $H'_{CP43-RC}$. $H'_{CP47-CP43}$ is the transpose of $H'_{CP43-CP47}$. H_{M1-M2} and H_{M2-M1} are 37 by 37 matrixes.

H_{RC} , H_{CP47} and H_{CP43} are Frenkel exciton Hamiltonian for RC, CP47 and CP43.

These are given as:

$$H_{RC} = \sum_{n=1}^8 E_n |n\rangle \langle n| + \sum_{n=1, n < m}^8 J_{nm} (|n\rangle \langle m| + |m\rangle \langle n|), \quad (3.1)$$

$$H_{CP47} = \sum_{n=9}^{24} E_n |n\rangle \langle n| + \sum_{n=9, n < m}^{24} J_{nm} (|n\rangle \langle m| + |m\rangle \langle n|), \quad (3.2)$$

$$H_{CP43} = \sum_{n=25}^{37} E_n |n\rangle \langle n| + \sum_{n=25, n < m}^{37} J_{nm} (|n\rangle \langle m| + |m\rangle \langle n|), \quad (3.3)$$

where E_n is the average site energies of pigment n obtained from MD trajectory.

$H_{CP47-RC}$, $H_{CP43-RC}$, $H_{CP43-CP47}$, $H_{RC-CP47}$, $H_{RC-CP43}$, and $H_{CP47-CP43}$ are off-diagonal term of the system Hamiltonian and all of the matrix elements are excitonic couplings between pigments of different complexes within a monomer. For example, matrix elements of $H_{CP47-RC}$ are excitonic couplings between pigments in CP47 and pigments in RC. These are given as:

$$H_{CP47-RC} = \sum_{n=9}^{24} \sum_{m=1}^8 J_{nm} |n\rangle \langle m| = (H_{RC-CP47})^T, \quad (3.4)$$

$$H_{CP43-RC} = \sum_{n=25}^{37} \sum_{m=1}^8 J_{nm} |n\rangle \langle m| = (H_{RC-CP43})^T, \quad (3.5)$$

$$H_{CP43-CP47} = \sum_{n=25}^{37} \sum_{m=9}^{24} J_{nm} |n\rangle \langle m| = (H_{CP47-CP43})^T. \quad (3.6)$$

Above block Hamiltonians describe one of monomers in PSII core complex. Block Hamiltonians with apostrophe describe the other monomer in PSII core complex. To distinguish two monomers, two monomers denote as monomer1 (M1) and monomer2 (M2). For example, H_{RC} is Frenkel Hamiltonian for RC in the M1, while H'_{RC} is Frenkel Hamiltonian for RC in the M2. The form of H_{RC} and H'_{RC} are the same, but values of matrix elements are slightly different. These are given as:

$$H'_{RC} = \sum_{n=38}^{45} E_n |n\rangle \langle n| + \sum_{n=38, n < m}^{45} J_{nm} (|n\rangle \langle m| + |m\rangle \langle n|), \quad (3.7)$$

$$H'_{CP47} = \sum_{n=46}^{61} E_n |n\rangle \langle n| + \sum_{n=46, n < m}^{61} J_{nm} (|n\rangle \langle m| + |m\rangle \langle n|), \quad (3.8)$$

$$H'_{CP43} = \sum_{n=62}^{74} E_n |n\rangle \langle n| + \sum_{n=62, n < m}^{74} J_{nm} (|n\rangle \langle m| + |m\rangle \langle n|). \quad (3.9)$$

$$H'_{CP47-RC} = \sum_{n=46}^{61} \sum_{m=38}^{45} J_{nm} |n\rangle \langle m| = (H'_{RC-CP47})^T, \quad (3.10)$$

$$H'_{CP43-RC} = \sum_{n=62}^{74} \sum_{m=38}^{45} J_{nm} |n\rangle \langle m| = (H'_{RC-CP43})^T, \quad (3.11)$$

$$H'_{CP43-CP47} = \sum_{n=62}^{74} \sum_{m=46}^{61} J_{nm} |n\rangle \langle m| = (H'_{CP47-CP43})^T. \quad (3.12)$$

H_{M1-M2} are off-diagonal term of the system Hamiltonian, too. It is a 37 by 37 matrix. However, matrix elements in H_{M1-M2} are excitonic couplings between pigments in two monomers. H_{M1-M2} is given as:

$$H_{M1-M2} = \sum_{n=1}^{37} \sum_{m=38}^{74} J_{nm} |n\rangle \langle m| = (H_{M2-M1})^T. \quad (3.13)$$

So far, we introduce that the system Hamiltonian includes average site energies of pigments and excitonic coupling based on crystal structure. Also, energy gap fluctuations is caused by the interaction between the system and the bath. The trajectory of energy gap fluctuation can calculate the energy gap auto-correlation function. Furthermore, quantum time correlation function is obtained by quantum correction of the energy gap auto-correlation function. Therefore, we have already constructed the effective model for PSII core complex. However, how can we trust the dynamics given by our model? We verify our model by fitting the absorption spectra. If our model can reflect the spectral properties, we have confidence in our model. In the following subsections, we present the simulation of absorption spectra based on our model. Also, we show site energies, excitonic couplings, exciton states, delocalization length and spatial delocalization for each complexes in PSII core complex. The site energy of pigments is average result from previous MD simulation and is verified by fitting absorption spectra. We apply transition charge for electrostatic potential (TrEsp) method to calculate excitonic coupling. Since most of exciton states delocalize at pigments within 30 Å, we consider the excitonic coupling only if the distance between pigments is less than 30 Å. In this work, we employ the PSII core complex crystal structure as structure reference [13]. Excitonic couplings showed in subsection 3.2.2 - 4.2 are average results.

3.2 An effective model for RC

3.2.1 Calibration of H_{RC}

In the H_{RC} , because we didn't have the site energies of pheophytins from MD, we take Renger's group as reference [23]. We apply average values of H_{RC} and H'_{RC} to simulate the absorption spectrum. Figure 3.3 is the simulation of the absorption spectrum based on original data of site energies for RC at 297 K. Peaks with dashed lines are contribution of each exciton states. Exciton states are labeled as e1 to e8, according to the transition energies from the lowest-energy state to the highest-energy state. We can discover that the range of exciton energies and broadening of peaks are too small. According to Eq. 2.12, it can be explain by the bias from the atomic transition charges obtained by TDDFT, background partial charges obtain by MD and the effective dielectric constant.

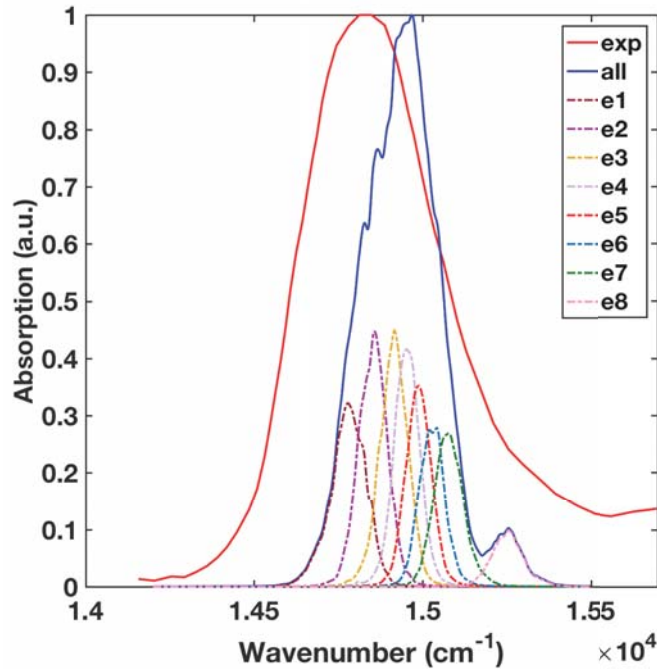


Figure 3.3: The simulated absorption spectrum of the PSII RC based on raw MD data. The red peak is the experimental result. The blue peak is the summation of contribution from all of the exciton states. Peaks with dashed lines are contribution of each exciton states.

Therefore, we multiply the site energies from MD data by a scaling factor, f . According to Eq. 2.11 and Eq. 2.12, the scaled site energy of the n^{th} site is given by

$$E_n^s = E_0 + \Delta E_n^s, \quad (3.14)$$

$$\Delta E_n^s(\tau) = f \Delta E_n(\tau) = \frac{f}{\epsilon_{eff}} \sum_i \sum_j \frac{\Delta q_i^n q_j^{bg}}{|r_i^n(\tau) - r_j^{bg}(\tau)|}, \quad (3.15)$$

where f is the scaling factor. ϵ_{eff} is the effective dielectric constant. Δq_i^n is the difference of ground state and excited state atomic partial charge i in the site n and q_j^{bg} is the background partial charge of charged residue j . r_i^n and r_j^{bg} are the position vectors of each atoms. Then, the modified classical time correlation function, $C_{MD}(\tau)$, is Eq. 2.18 multiplied by f^2 :

$$C_{MD}(\tau) = f^2 C_{MD}^{avg} = \frac{f^2}{N} \sum_n \langle \delta E_n(\tau) \delta E_n(0) \rangle \quad (3.16)$$

where C_{MD}^{avg} average classical time correlation function of each sites in the RC and $\delta E_n(\tau) = \Delta E_n(\tau) - \overline{\Delta E_n}$. When the classical time correlation function is tuned, the absorption line shape function is tuned simultaneously. After multiply by a scaling factor, $f=5$, the width of simulation peak gets close to the experiment. However, the average energy of 8th exciton state are far away from others. Special pair mainly contributes to this state. In the CDC method, it assumes pigments are independent to each other. This assumption isn't suitable for special pair, because the distance of special pair is very close and they strongly couple. It leads to a bad estimation of site energies. So we take special pair site energies and coupling between them as parameters. In addition, two pheophytin site energies are also parameters. Finally, the simulation is similar to the experiment.

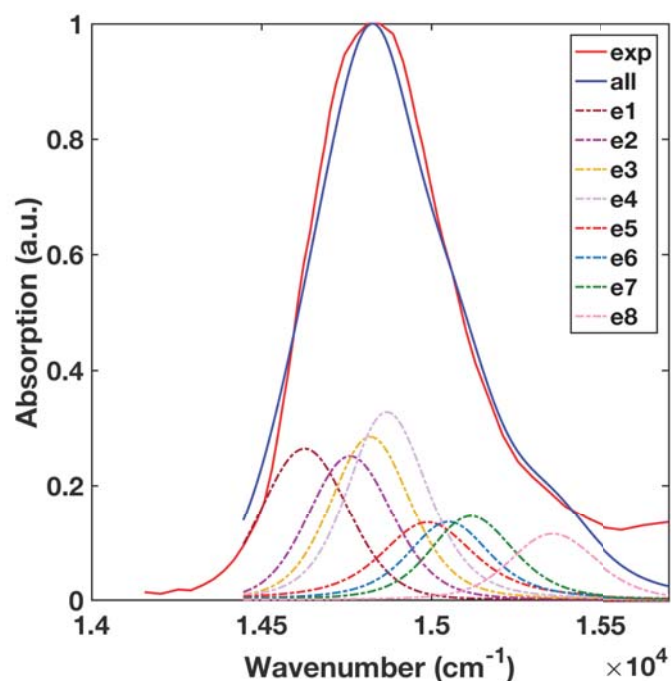


Figure 3.4: The simulated absorption spectrum of the PSII RC after the correction. The scaling factor is five. The red peak is the experimental result. The blue peak is the summation of contribution from all of the exciton states. Peaks with dashed lines are contribution of each exciton states.

3.2.2 Frenkel exciton Hamiltonian of RC

In this subsection, we focus on the RC. We diagonalize the average result of H_{RC} and H'_{RC} to obtain exciton states at RC. Site energies with respect to the average energy of 74 pigments (14936 cm^{-1}) are shown in Fig. 3.5 .

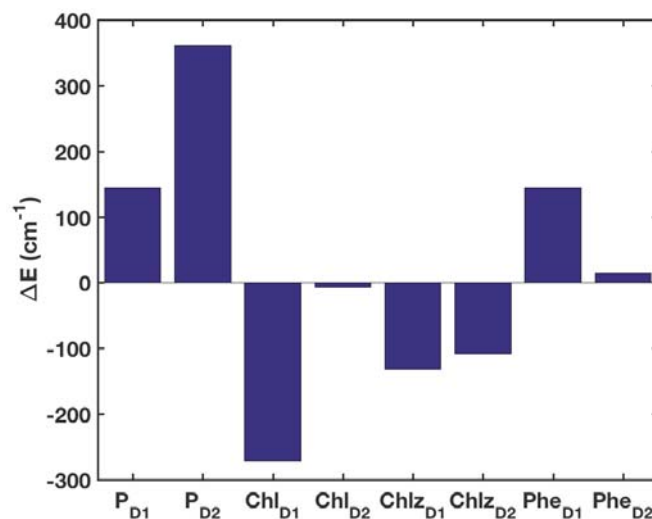


Figure 3.5: Average site energies of each pigments in the RC. X axis is the label of each pigments in the RC. Y axis is the relative site energies with respect to the average energy of 74 pigments.

The Chl_{D1} has the lowest site energy. It agrees with the previous literatures [23, 6, 16]. Peripheral chlorophylls a, the $Chlz_{D1}$ and the $Chlz_{D2}$, also have lower site energies. The site energy difference of the Chl_{D2} and the Phe_{D2} is only 20.73 cm^{-1} , which lead to mixing of these two pigments in exciton states. It will be mentioned bellow. Special pair and Phe_{D1} have higher site energies. The order from low energy to high energy is the P_{D1} , the Phe_{D1} and then the Phe_{D2} . In previous literatures, some give the P_{D1} a higher site energy than the P_{D2} [23, 16], while Fleming's group gives special pair same site energies [6]. However, MD simulation gives a different tendency, which the site energy of the P_{D2} is 216.58 cm^{-1} higher than the P_{D1} . The site energy difference of special pair is larger than previous studies and it cause that we need to lower the excitonic coupling of special pair to 100 cm^{-1} .

Figure 3.6a and Fig. 3.6b show excitonic couplings and exciton states at the RC. The color in Fig. 3.6b represent the contribution, $(|C_n^\alpha|)^2$, of the pigment.

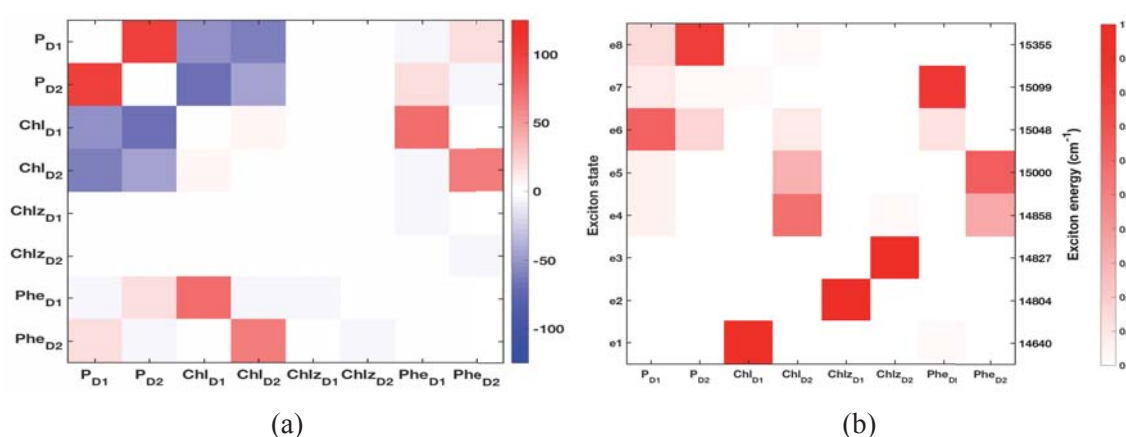


Figure 3.6: Excitonic couplings and exciton states in the RC. (a) Excitonic couplings of pigments at the RC. X axis and y axis are the label of each pigments in the RC. Red is the positive value for excitonic coupling. Blue is the negative value for excitonic coupling. (b) Exciton states in the RC. X axis is the label of each pigments in the RC. Y axis is the label of each exciton states and the transition energies for each exciton states.

The order of the most contribution site from the lowest-energy exciton state to the highest-energy exciton state is equal to the order of site energies. The lowest-energy exciton state, e1, is mainly contributed by the Chl_{D1} . The other pigment contributing to this state is made by the Phe_{D1} which is strongly coupled to the Chl_{D1} (74.13 cm^{-1}) due to its proximity (13.41 \AA). The Phe_{D1} is the major contributors to the higher-energy exciton

state, e7. For this reason, the excitation energy flows to the Phe_{D1} and then could flow to the Chl_{D1} directly. The states, e2 and e3, localize at two peripheral chlorophylls a, respectively. The distance of two peripheral chlorophylls a and the others are far and it gives rise to weakly couple to other pigments. The states, e4 and e5, have contributions from the P_{D1} , the Chl_{D2} and the Phe_{D2} and the $Chlz_{D1}$ only contribute to the state, e4. The contributions of the states, e6 and e8, are special pair and the Chl_{D2} . Also, the Phe_{D1} contributes to the state e8. The states e4 to e8 are delocalize more than one pigments. For this reason, excitation energies can transport between these states quickly and it isn't the bottleneck for the charge transfer.

In order to quantify the degree of delocalization, we calculate the delocalization length of each state, L_α . It is defined as

$$L_\alpha = \left(\sum_n |C_n^\alpha|^4 \right)^{-1} \quad (3.17)$$

The delocalization lengths of e4 to e6 are about 2. However, the delocalization lengths of e7 and e8 are about 1.4 and the delocalization lengths of e1 to e3 are close to 1. It means that most states at RC are localized at up to two pigments. Nevertheless, the delocalization length can't tell us how one state distribute in real space. So, we also calculate the spatial delocalization which can show the degree of delocalization in real space. First, we apply the crystal structure to calculate the average location of each states. The location of n^{th} site is represented by the central magnesium atom and denote as \mathbf{R}_n . So, the average location of α^{th} state, $\langle \mathbf{R}^\alpha \rangle$, is

$$\langle \mathbf{R}^\alpha \rangle = \sum_n |C_n^\alpha|^2 \mathbf{R}_n \quad (3.18)$$

Then, Spatial delocalization, $\langle \Delta \mathbf{R}^\alpha \rangle$, is defined as

$$\langle \Delta \mathbf{R}^\alpha \rangle = \sqrt{\sum_n |C_n^\alpha|^2 (\mathbf{R}_n - \langle \mathbf{R}^\alpha \rangle)^2} \quad (3.19)$$

The results given in table 3.1. We can see that the exciton states are delocalized at

about 4.5 Å in standard deviation. Comparing to the nearness neighbor of inter-chlorophyll distance, which is about 10 Å, the excitons are more or less localized on one chlorophyll.

Table 3.1: The delocalization of exciton states in the RC

	e1	e2	e3	e4	e5	e6	e7	e8
Delocalization length	1.10	1.00	1.04	2.20	1.96	2.21	1.35	1.46
Spatial delocalization (Å)	2.34	0.79	3.31	6.77	6.06	6.74	5.41	3.56

3.3 Effective models for CP47 and CP43

3.3.1 Calibration of H_{CP47} and H_{CP43}

To verify our model, we also simulate absorption spectra of antenna complexes. We apply average values of H_{CP47} and H'_{CP47} to simulate the absorption spectrum of CP47. The absorption spectrum of CP43 are average values, too. First, we multiply site energies and the quantum time correlation function by a scaling factor, $f=5$. However, the spectral widths of the CP43 and the CP47 are too broad to fit absorption spectrums. Therefore, we try to scale site energies and C_{MD}^{avg} individually. We find that site energies obtained from MD structure of the CP43 and the CP47 don't need to multiply by a scaling factor, but the time correlation function should be multiplied by the scaling factor, $f=5$.

Figure 3.7a and Figure 3.7b show results of the CP43 and the CP47. The absorption spectrum of the CP43 shows a great fitting with the experimental result. The absorption spectrum of the CP47 based on simulation have an unapparent shoulder around 15200 cm^{-1} , but still gives a similar shape. After fitting the absorption spectra of CP43, CP47 and RC, we have confidence in our Frenkel exciton model for PSII core complex.

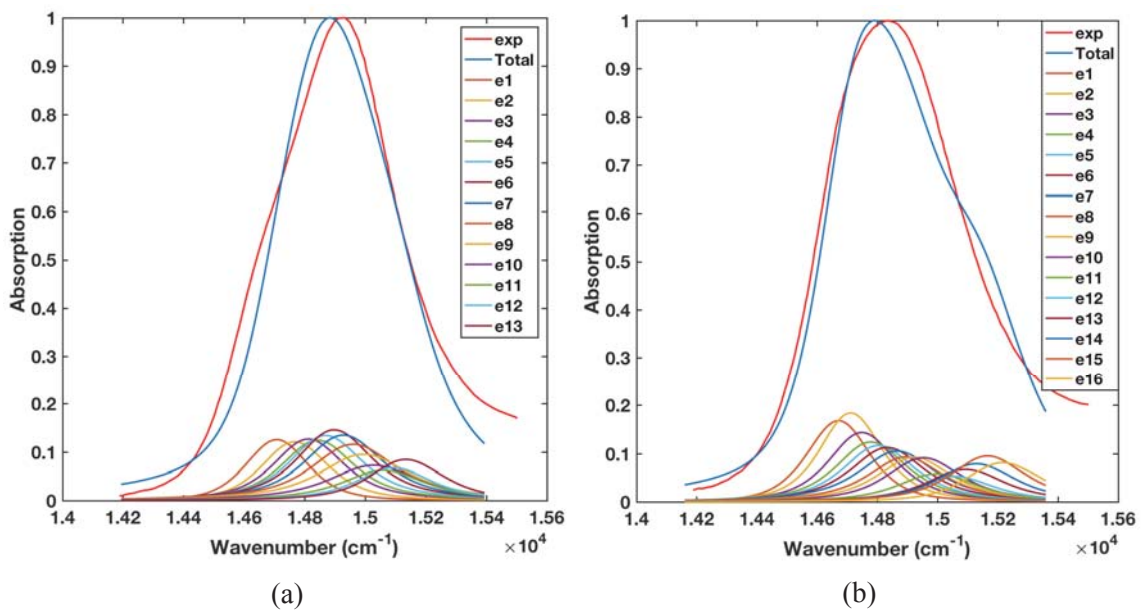


Figure 3.7: (a) The absorption spectrum of the CP43 (b)The absorption spectrum of the CP47

3.3.2 Frenkel exciton Hamiltonian of CP47

In this subsection, we focus on the CP47. We diagonalize the average result of H_{CP47} and H'_{CP47} to obtain exciton states at CP47. Site energies with respect to the average energy of 74 pigments (14936 cm^{-1}) are shown in Fig. 3.8a.

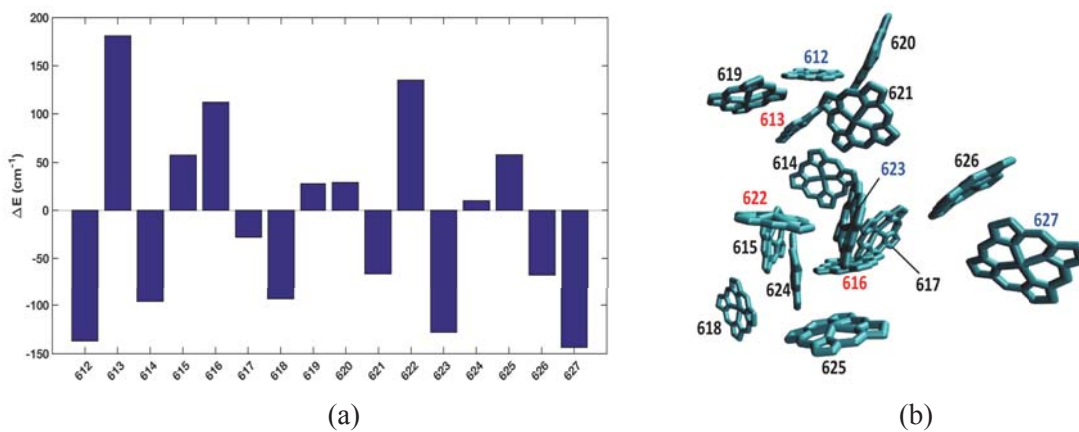


Figure 3.8: Average site energies and positions of each pigment in the CP47. (a) Average site energies of each pigment in the CP47. X axis is the label of each pigment in the CP47. Y axis is the relative site energies with respect to the average energy of 74 pigments. (b) Positions of each pigments in the CP47. Red labels represent three higher-energy sites. Blue labels represent three lower-energy sites.

CLA627 and CLA612 have the lowest site energies. It agrees with the previous literatures [23, 6, 48]. CLA623 also have the lower site energy. The site energy difference of

CLA619 and CLA620 is only 1.34 cm^{-1} , which lead to mixing of these two pigments in exciton states. CLA613, CLA616 and CLA622 have higher site energies. The order from low energy to high energy is CLA616, CLA622 and then CLA613. Figure 3.8b shows positions of pigments in the CP47. We discover that two pairs of higher-energy sites and lower-energy sites are neighbors. The distance between CLA614 and CLA613 is 8.59 \AA and the distance between CLA622 and CLA623 is 8.81 \AA . A closer distance may leads to a stronger excitonic coupling. Then, excitation energy transfer may takes place between exciton states contributed from these pigments.

Figure 3.9a and Fig. 3.9b show excitonic couplings and exciton states at the CP47. The color in the figure 3.9b represent the contribution, $|C_n^\alpha|^2$, of the pigment. The lowest-energy exciton state, e1, is mainly contributed by CLA623 rather than CLA627. CLA623 is coupled to CLA621, CLA624 and CLA625, so the energy of exciton state contributed by CLA623 is lower than the site energy of CLA623 and CLA627. We can find that although the distance of CLA622 and CLA623 are very close, the excitonic coupling between them is only 1.64 cm^{-1} . The reason is that transition dipole of CLA622 are approximately perpendicular to the transition dipole of CLA623, so excitonic coupling become very small. In Fig. 3.9a, excitonic couplings of pigments in the CP47 and CLA627 are very small. Therefore, the state e3 contributed by CLA627 are localized at CL627.

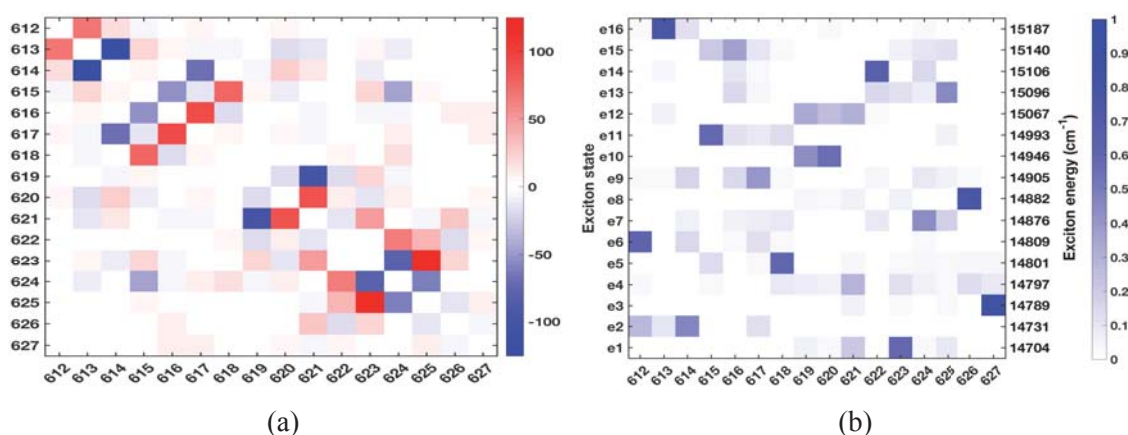


Figure 3.9: Excitonic couplings and exciton states in the CP47. (a) Excitonic couplings of pigments at the CP47. X axis and y axis are the label of each pigments in the CP47. Red is the positive value for excitonic coupling. Blue is the negative value for excitonic coupling. (b) Exciton states in the CP47. X axis is the label of each pigments in the CP47. Y axis is the label of each exciton states and the transition energies for each exciton states.

The highest-energy state, e16, is mainly contributed by CLA613. The other pigment contributing to this state is made by CLA614 which is strongly coupled to CLA613 (-125.47 cm^{-1}) due to its proximity mentioned above. Also, CLA614 is the major contributors to the lower-energy exciton state, e2. Therefore, the excitation energy flows from the state e16 to the state e2 may very fast and directly due to the spatial overlap between these exciton states.

In the table 3.2, it shows the delocalization length and spatial delocalization of exciton states in the CP47. The site energy range in the CP47 is more closer than in the RC. It leads to a higher average delocalization length about 3.10. In addition, the state e4 have the highest delocalization length (6.71), but spatial delocalization of e4 is only 13.99 Å. That is, the state e4 are more or less localized on about two or three pigments. Also, the delocalization length of the exciton state e6 is 2.37, but spatial delocalization of e4 is 13.26 Å. The reason is that the distance of CLA612 and CLA614 is 17.93 Å, so spatial delocalization becomes larger.

Table 3.2: The delocalization of the RC

	e1	e2	e3	e4	e5	e6	e7	e8
Delocalization length	2.55	3.16	1.37	6.71	2.58	2.37	4.08	1.71
Spatial delocalization (Å)	8.69	10.04	8.45	13.99	12.63	13.26	12.37	8.43
	e9	e10	e11	e12	e13	e14	e15	e16
Delocalization length	4.56	2.03	2.61	3.59	3.78	2.21	4.60	1.71
Spatial delocalization (Å)	12.83	8.57	9.59	9.13	11.59	10.45	11.00	7.61

3.3.3 Frenkel exciton Hamiltonian of CP43

In this subsection, we focus on the CP43. We diagonalize the average result of H_{CP43} and H'_{CP43} to obtain exciton states at CP43. Site energies with respect to the average energy of 74 pigments (14936 cm^{-1}) are shown in Fig. 3.10a.

The site energy range in CP43 is narrow than CP47. The energy difference between the highest-energy state and the lowest-energy state is 185.23 cm^{-1} . CLA636 is the lowest-energy site. Previous studies also show that CLA636 has a lower site energy.

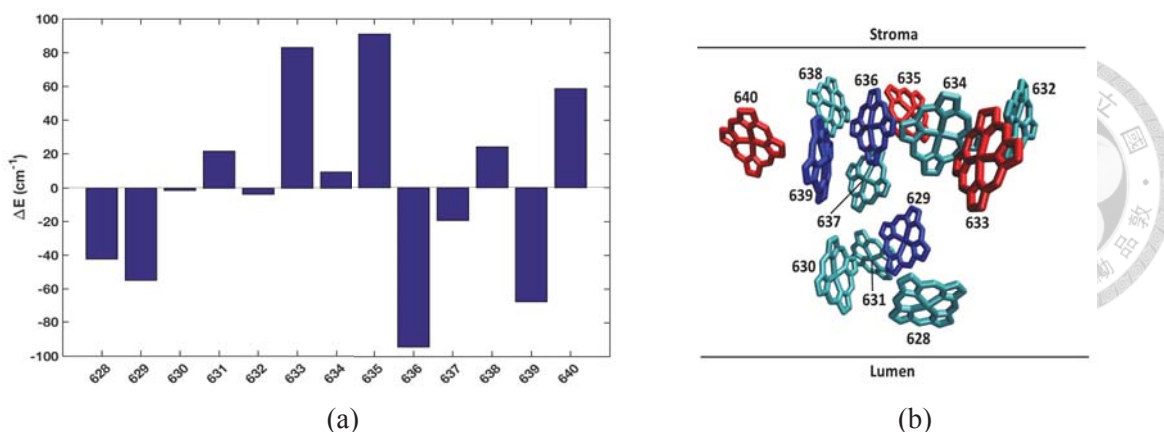


Figure 3.10: Average site energies and positions of each pigment in the CP43. (a) Average site energies of each pigment in the CP43. X axis is the label of each pigment in the CP43. Y axis is the relative site energies with respect to the average energy of 74 pigments. (b) Positions of each pigment in the CP43 in side view. Red chlorins represent three higher-energy sites. Blue chlorins represent three lower-energy sites.

CLA633, CLA635 and CLA640 are higher-energy sites. In Fig. 3.8b, these pigments are shown as red color. We can discover that they are close to the stroma side. We also find that two pairs of higher-energy sites and lower-energy sites are neighbors. The distance between CLA639 and CLA640 is 10.23 \AA and the distance between CLA635 and CLA636 is 9.04 \AA . However, due to the approximately perpendicular orientation of transition dipoles, the excitonic coupling between CLA639 and CLA640 is -41.47 cm^{-1} and the excitonic coupling between CLA635 and CLA636 is 21.74 cm^{-1} .

Figure 3.11a and Fig. 3.11b show excitonic couplings and exciton states in the CP43. The lowest-energy exciton state, e1, is mainly contributed by CLA636. The other pigment contributing to this state is made by CLA638 which is strongly coupled to the CLA636 (119.26 cm^{-1}). CLA638 is the major contributors to the highest-energy exciton state, e13. It leads to the fast energy transfer rate from the state e13 to the state e1. In Fig. 3.11a, we can find that CLA629-CLA631, which are in the lumen side, are coupled to each other. Also, Both of them are coupled to CLA637, which like a bridge between the stroma side and the lumen side. The exciton state, e2, is mainly contributed by CLA629 and CLA637. CLA637 contribute to higher-energy states, e12 and e13 and CLA629 contribute to states, e9 and e10. For this reason, the excitation energy can flows from the state e13 to lower-energy states directly due to spatial overlap of these states. Therefore, in the CP43,

excitation energy distribution may reach Boltzmann distribution quickly.

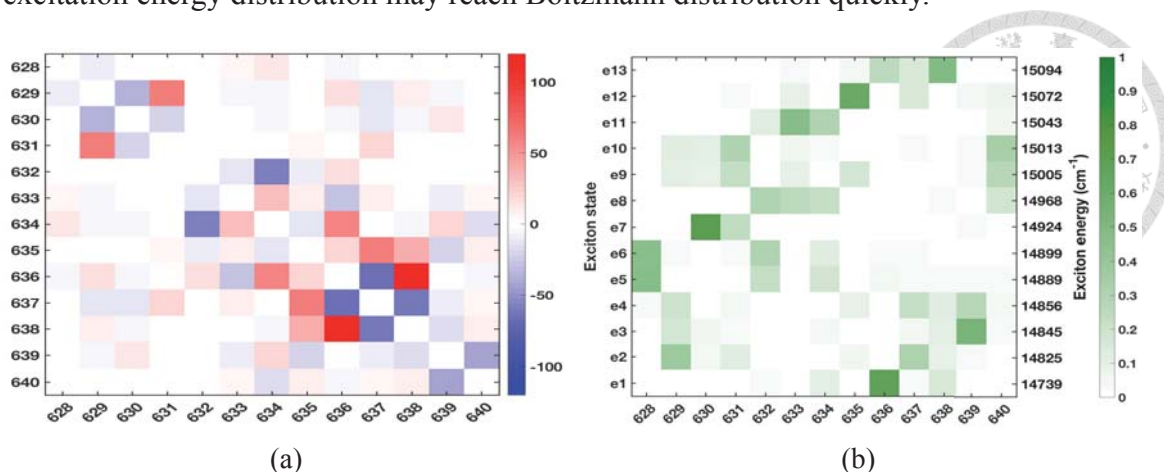


Figure 3.11: Excitonic couplings and exciton states in the CP43. (a) Excitonic couplings of pigments at the CP43. X axis and y axis are the label of each pigments in the CP43. Red is the positive value for excitonic coupling. Blue is the negative value for excitonic coupling. (b) Exciton states in the CP43. X axis is the label of each pigments in the CP43. Y axis is the label of each exciton states and the transition energies for each exciton states.

In the table 3.3, it shows the delocalization length and spatial delocalization of exciton states in the CP43. The average delocalization length about 3.41. In addition, the state e9 have the highest delocalization length (5.54) and the highest spatial delocalization (15.51 Å). This state delocalize on pigments in the stroma side and pigments in the lumen side. Since the average distance of nearest neighbors in the CP43 is 10.35 Å. Most of the exciton states are localized on one site, while some of them are delocalized on more than one site.

Table 3.3: The delocalization of the RC

	e1	e2	e3	e4	e5	e6	e7
Delocalization length	2.04	3.78	2.95	5.14	3.20	3.15	1.75
Spatial delocalization (Å)	6.94	8.99	11.30	11.49	12.60	12.54	7.95
	e8	e9	e10	e11	e12	e13	
Delocalization length	4.17	5.54	4.26	2.95	2.39	2.99	
Spatial delocalization (Å)	13.11	15.51	15.13	9.21	10.90	8.03	



Chapter 4

Effective model for PSII core complex monomer (C1)

4.1 Master equation and rate constant matrix based on MRT

In the chapter 3, we verify our effective model to determine effective Hamiltonian for the system and quantum time correlation function to describe the interaction of the system and the bath. Then, we can construct the rate constant matrix for exciton states in the PSII core complex. In the rate constant matrix for a monomer of PSII core complex, 37 exciton states are considered. The off-diagonal term of rate constant matrix is the population transfer rates, $R_{\alpha\alpha\beta\beta}$, between exciton states. $R_{\alpha\alpha\beta\beta}$ represent the transfer rate from the exciton state β to the exciton state α . The transfer rate is calculated by modified Redfield theory (MRT), which is mentioned in the chapter 2 [47]. The diagonal term, $R_{\alpha\alpha\alpha\alpha}$, is the inverse decay time for each exciton state. Therefore, $R_{\alpha\alpha\alpha\alpha}$ is summation of transfer rates from the exciton state α to other states and the inverse fluorescence lifetime, $\frac{1}{\tau_{FL}} = 1(ns^{-1})$, and is denoted by

$$R_{\alpha\alpha\alpha\alpha} = -\frac{1}{\tau_{FL}} - \sum_{\beta \neq \alpha}^{37} R_{\beta\beta\alpha\alpha}. \quad (4.1)$$

However, the direction of excitation energy transfer in PSII core complexes not only transports from high-energy states to low-energy states but also toward RCs, which is driven by the excitation depletion of the population by charge separation. We need to phenomenologically apply two charge separation rate of two pathways for primary charge separation, PD1 pathway and ChlD1 pathway, in our model. The detail is mentioned in the subsection 1.1.2. We only consider two apparent time constants for the formation of radical pair 1 (RP1), $Chl_{D1}^+Phe_{D1}^-$, and radical pair 2 (RP2), $P_{D1}^+Chl_{D1}^-$. τ_{RP1} is 700 fs and τ_{RP2} is 3 ps. In a monomer of PSII core complex, two radical pair states, RP1, and RP2 are labeled as e38, and e39, respectively. We assume that the exciton state, e1, mainly contributed by Chl_{D1} has the probability to become RP1 and the exciton state, e28, mainly contributed by P_{D1} has the probability to become RP2. Therefore, we considered two charge separation rates in the rate constant matrix and charge separation rates are

$$R_{RP1,RP1,e1,e1} = R_{38,38,1,1} = \frac{1}{\tau_{RP1}} = \frac{1}{700} (fs^{-1}), \quad (4.2)$$

$$R_{RP2,RP2,e28,e28} = R_{39,39,28,28} = \frac{1}{\tau_{RP2}} = \frac{1}{3} (ps^{-1}). \quad (4.3)$$

The others matrix elements are zero.

To extend to dimeric PSII core complex, 74 exciton states are considered in the rate constant matrix for PSII core complex. The off-diagonal term of rate constant matrix is the population transfer rates between exciton states. The diagonal term is the inverse decay time for each exciton state. We also need to consider charge separation rates. However, PSII core complex has two RC, so four radical pairs are considered. Four radical pairs, RP1 (M1), RP2 (M1), RP1 (M2), and RP2 (M2), is charge transfer states and are labeled as e75, e76, e77, and e78, respectively. We assume that the exciton states, e1 and e2, mainly contributed by Chl_{D1} have the probability to become RP1 and the exciton states, e53 and e56, mainly contributed by P_{D1} have the probability to become RP2. Therefore,

charge transfer rates is given by:

$$R_{RP1(M1),RP1(M1),e2,e2} = R_{75,75,2,2} = \frac{1}{\tau_{RP1}} = \frac{1}{700} (fs^{-1}), \quad (4.4)$$

$$R_{RP2(M1),RP2(M1),e53,e53} = R_{76,76,53,53} = \frac{1}{\tau_{RP2}} = \frac{1}{3} (ps^{-1}), \quad (4.5)$$

$$R_{RP1(M2),RP1(M2),e1,e1} = R_{77,77,1,1} = \frac{1}{\tau_{RP1}} = \frac{1}{700} (fs^{-1}), \quad (4.6)$$

$$R_{RP2(M2),RP2(M2),e56,e56} = R_{78,78,56,56} = \frac{1}{\tau_{RP2}} = \frac{1}{3} (ps^{-1}). \quad (4.7)$$

The others matrix elements are zero. The rate constant matrix with charge transfer rates for exciton states in PSII core complex denoted by $\mathbf{R}_{C2}^{(CT)}$.

With the rate constant matrix, we can apply master equation to propagate the excitation energy transfer dynamics. The master equation is given by:

$$\frac{dP(t)}{dt} = \mathbf{R}_{C2}^{(CT)} P(t), \quad (4.8)$$

$$P(t) = \sum_{\alpha=1}^{78} P_{\alpha}(t) |\alpha\rangle, \quad (4.9)$$

where $P_{\alpha}(t)$ is the population of the exciton state α at $T = t$. Given the initial condition of the population for exciton states, we can discover the dynamics in our model.

4.2 Exciton states and inter-complex excitonic couplings for PSII core complex monomer (C1)

In the chapter 3, we discuss Frenkel exciton Hamiltonians of each complex in the PSII. In this section, we introduce the excitonic coupling of pigments within CP47, CP43, and RC and then we can discuss exciton states based on Frenkel exciton Hamiltonian of monomers in the PSII.

Figure 4.1 shows the excitonic coupling between antenna complexes, CP47 and CP43, and a RC. The maximum value of a color bar in Fig. 4.1a is 8.5 cm^{-1} and the maximum

value of a color bar in Fig. 4.1b is 6.5 cm^{-1} . That is to say, excitonic couplings between a CP47 or CP43 and a RC is weaker than excitonic couplings within a CP47, CP43 or RC. Therefore, exciton states may retain the exciton state character in the H_{RC} , H_{CP47} , and H_{CP43} . It is showed in Fig. 4.2. In Fig. 3.1, we can discover that the CP47 closes to $Chlz_{D2}$, Phe_{D2} , and P_{D2} . It can also find in Fig. 4.1a, which shows the exciton states in a monomer. The excitonic coupling between pigments in D2 protein chain of the RC and pigments in the CP47 are stronger. The CP43 closes to $Chlz_{D1}$, Phe_{D1} , and P_{D1} , so similar patterns are showed in Fig. 4.1b. We don't show the excitonic coupling between the CP47 and CP43, because excitonic couplings between them are too small to be considered.

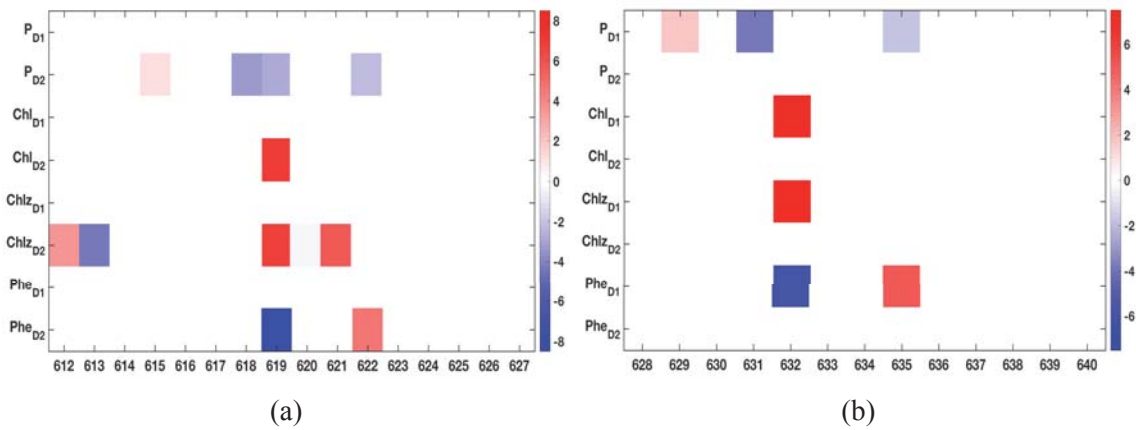


Figure 4.1: Excitonic couplings of pigments between antenna complexes, CP47 and CP43, and a RC. (a) Excitonic couplings of pigments between a CP47 and a RC. X axis is the label of each pigments in the CP47. Y axis is the label of each pigments in the RC. Red is the positive value for excitonic coupling. Blue is the negative value for excitonic coupling. (b) Excitonic couplings of pigments between a CP43 and a RC. X axis is the label of each pigments in the CP43. Y axis is the label of each pigments in the RC. Arrows indicate the contribution of pigments from different complexes.

In Fig. 4.1, we can find that two of the exciton states, which are most contributed from pigments in the RC, are contributed from pigments in antenna complexes. The state e11 is mainly contributed by $Chlz_{D2}$, which is coupled to CLA612, and is also contributed by CLA612. CLA612 is the major contributors to the exciton state, e19. It may leads to excitation energy transfer from the RC to CP47 by the state e9 and the state e11. The state e33 is mainly contributed by Phe_{D1} , which is coupled to CLA635 ($4,97 \text{ cm}^{-1}$), and leads to CLA635 contribute to the state e33. CLA635 is the major contributors to the exciton

state, e30. The state e30 is also contributed by Phe_{D1} . Therefore, excitation energy transfer between these states may very fast. It results in energy transfer from the CP43 to the RC. The state e6 is delocalized on few pigments in the CP47. $Chlz_{D2}$ contributes to the state e6, too. It also leads to excitation energy transfer from the RC to the CP47.

The exciton state in a monomers is similar to the exciton state in each complex. There are only a few states are contributed by pigments in a RC and an antenna complex. These states may be key states for excitation energy transfer between complexes.

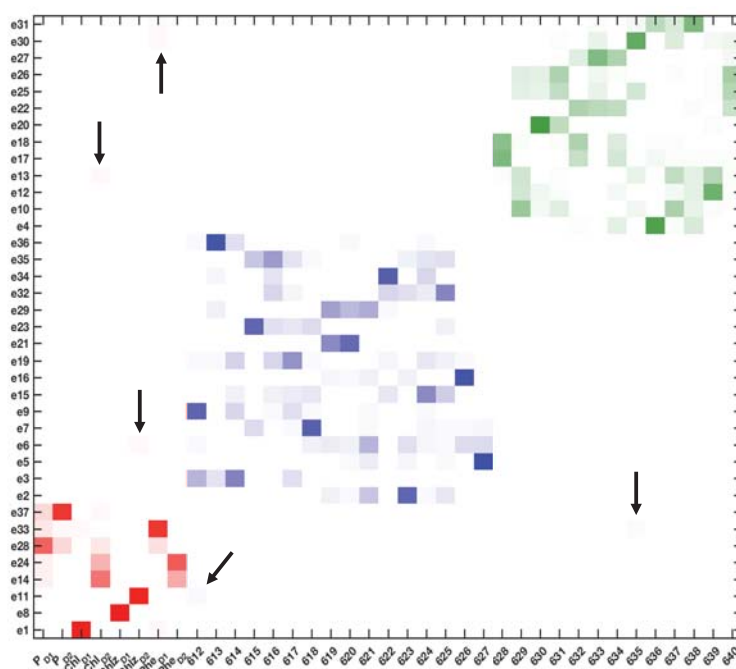
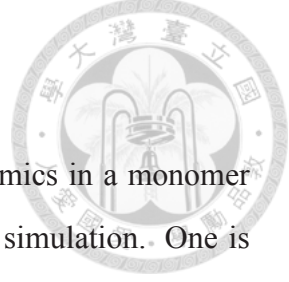


Figure 4.2: Exciton states in a monomer of PSII. X axis is the label of each pigments in a monomer and from left to right are pigments of RC, CP47 and CP43. Y axis is the label of exciton states in a monomer. The lowest-energy state is labeled as e1 and the highest-energy state is labeled as e37. Colored squares shows the contribution, $|C_n^\alpha|^2$, of pigments n in a exciton state α . Red is the contribution of pigments in the RC. Blue is the contribution of pigments in the CP47. Green is the contribution of pigments in the CP43. The color bar for each color are the same and is from 0 to 1. The darker the color, the larger the value.

4.3 Excitation energy transfer dynamics in a monomer of PSII core complex(C1)



In this section, we discover the excitation energy transfer dynamics in a monomer of PSII core complex. Two initial conditions are considered in our simulation. One is initial excitation at the CP47. That is, we assume equal population of the exciton states, which are mainly contributed by pigments in the CP47, as the initial condition. The other is initial excitation at the CP43. Figure 4.3 shows the excitation energy transfer dynamics with initial excitation at the CP47.

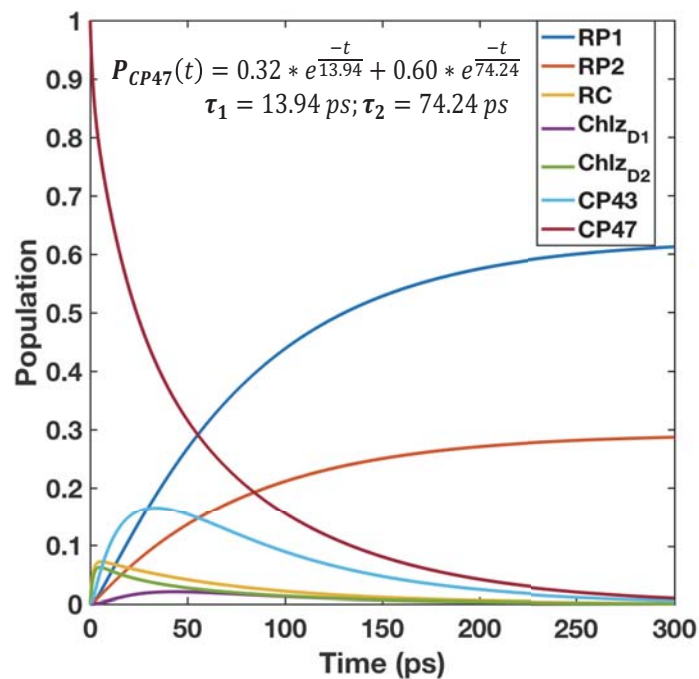


Figure 4.3: Excitation energy transfer with initial excitation at the CP47. Brown line is the population of exciton states which are mainly contributed by pigments in the CP47. Cyan line is the population of exciton states contributed by pigments in the CP43. Green line is the population of the exciton state contributed by $Chlz_{D2}$. Purple line is the population of the exciton state contributed by $Chlz_{D1}$. Yellow line is the population of exciton states contributed by pigments in the RC excluding $Chlz_{D1}$ and $Chlz_{D2}$. Blue line is the population of RP1. Orange line is the population of RP2.

The fitting function based on two exponential decays is showed in the figure. When the population of the CP47 decay rapidly, the population of the CP43 is increasing and reach the maximum of about 0.15. It implies that excitation energy may transfer from the CP47 to the CP43 by passing through the RC because the CP47 and the CP43 aren't

adjacent in space and the excitonic couplings of pigments between the CP47 and the CP43 are zero. Also, in the subsection 4.2, we mentioned that excitation energy transfer from the RC to the CP47 may takes place. In the rate constant matrix, we can find that the transfer rate from exciton state e11, contributed by $Chlz_{D2}$, to the exciton state e6, contributed by pigments in the CP47, is 14.61 ps and the rate from the state e11 to the state e9, contributed by pigments in the CP47, is 21.05 ps. There are the evidence for energy transfer from the RC to the CP47. At 300 ps, most of the exciton states become radical pairs. We define the quantum yield of charge transfer as the summation of populations for radical pairs at $T = 300$ ps. The population of RP1 is 0.63 and the population of RP2 is 0.29. The quantum yield of charge transfer is 0.92. The dynamics reproduce the high quantum yield of charge transfer in the PSII.

Figure 4.4 shows the excitation energy transfer dynamics with initial excitation at the CP43. The fitting function based on two exponential decays is showed in the figure. When the population of the CP43 decay rapidly, the population of the CP47 is increasing and reach the maximum of about 0.25. It implies that excitation energy may transfer from the CP43 to the CP47 by passing through the RC, too. At 300 ps, most of the exciton states become radical pairs. The population of RP1 is 0.66 and the population of RP2 is 0.26. The quantum yield of charge transfer is 0.92. We plot the population of $Chlz_{D1}$ and the population of $Chlz_{D2}$ individually. We want to investigate that whether excitation energy must transfer from peripheral chlorophyll to the core of RC. In Fig. 4.4, we can discovered that the population of the RC increases faster than the population of $Chlz_{D1}$. Therefore, excitation energy transfer from antenna complexes to RC can be achieved without passing though $Chlz$.

In our model, excitation energy in the reaction center can flow out of the RC and go to the CP47 or the CP43. That is, the energy transfer to the RC is reversible. In addition, the time scale of energy transfer from antenna complexes to the RC is less than 100 ps, so the time scale of fluorescence can't compete with the time scale of energy transfer. It lead to the high quantum yield of charge separation in the RC.

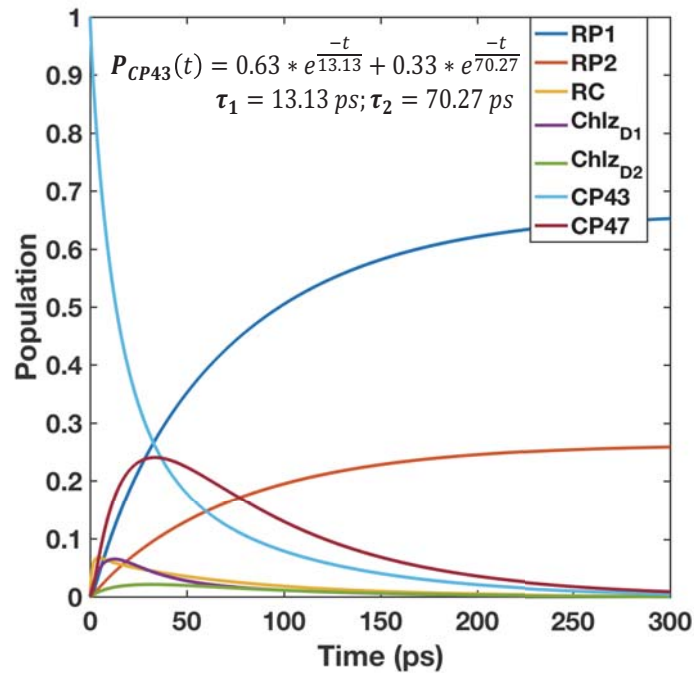


Figure 4.4: Excitation energy transfer with initial excitation at the CP43. Brown line is the population of exciton states which are mainly contributed by pigments in the CP47. Cyan line is the population of exciton states contributed by pigments in the CP43. Green line is the population of the exciton state contributed by $Chlz_{D2}$. Purple line is the population of the exciton state contributed by $Chlz_{D1}$. Yellow line is the population of exciton states contributed by pigments in the RC excluding $Chlz_{D1}$ and $Chlz_{D2}$. Blue line is the population of RP1. Orange line is the population of RP2.



Chapter 5

An effective model for PSII core complex (C2)

5.1 Exciton states and inter-monomer excitonic couplings for PSII core complex (C2)

Finally, we discuss the exciton states in whole PSII core complex. Site energies for each pigments in a dimer are the average results from MD for each pigments. Also, excitonic couplings are based on crystal structure and the excitonic couplings for the same labeled pigments in two monomers are slightly different. As mentioned in section 4, we consider the excitonic coupling only if the distance between pigments is less than 30 Å. To avoid non-physical delocalization in pigments with large distance due to energetic degeneracy, we consider another constraint. If the absolute value of the ration of excitonic coupling to the site energy difference between two pigments, $|\frac{J_{nm}}{\Delta E_{nm}}|$, is larger than 1 and the site energy difference is smaller than 10 cm^{-1} , we assume the excitonic coupling between pigment n and m is zero. Therefore, there are only three excitonic couplings considered in inter-monomer excitonic couplings, $J_{Chlz_{D1}(M1)-CLA616(M2)}$, $J_{Chlz_{D1}(M2)-CLA616(M1)}$, and $J_{CLA625(M1)-CLA625(M2)}$. However, $J_{Chlz_{D1}(M1)-CLA616(M2)}$ is only -0.01 cm^{-1} . $J_{CLA625(M1)-CLA625(M2)}$ is 5.14 cm^{-1} and is the only inter-monomer excitonic coupling to affect the property of exciton states in the PSII, because they are the nearest between

monomers with 29 Å.

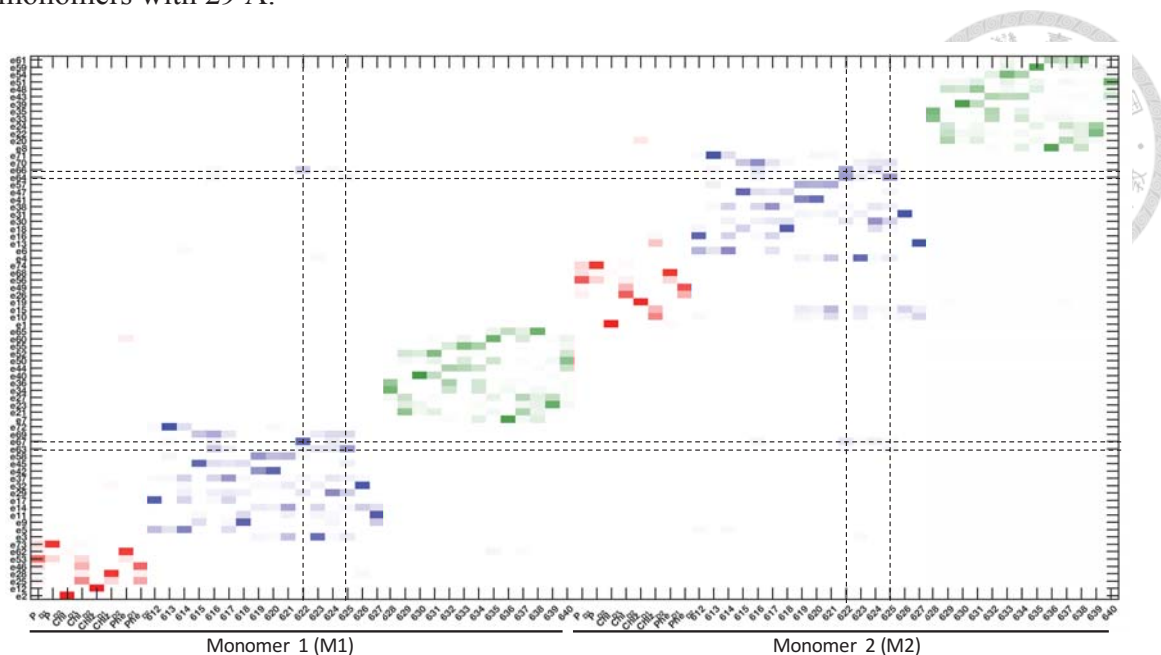


Figure 5.1: Exciton states in the PSII core complex. X axis is the label of each pigments in the PSII core complex and from left to right are pigments of RC, CP47 and CP43 in the M1 and then pigments of RC, CP47 and CP43 in the M2. Y axis is the label of exciton states in the PSII core complex. The lowest-energy state is labeled as e1 and the highest-energy state is labeled as e74. Colored squares shows the contribution, $(|C_n^\alpha|)^2$, of pigments n in a exciton state α . Red is the contribution of pigments in the RC. Blue is the contribution of pigments in the CP47. Green is the contribution of pigments in the CP43. The color bar for each color are the same and is from 0 to 1. The darker the color, the larger the value.

In Fig. 5.1, we can find that the states, e63, e64, e66, and e67, are contributed by pigments in two CP47s. The main contribution of state e63 is CLA625 in the M1, while CLA625 in the M2 also contributes to the state e63. In addition, CLA625 in the M2 contributes to the state e64. Moreover, The state e67 is mainly contributed by CLA622 in the M1. We can also find the contributions of CLA622 to CLA625 in the M2 for the state e67 and CLA622 in the M2 contributes to the state e66. The reason is that excitonic coupling of CLA622 and CLA625 in a CP47 is strong enough (39 cm^{-1}), so the exciton states contributed by CLA625 (M1) or CLA625 (M2) can couple to CLA622(M1) or CLA622(M2). The inter-monomer excitation energy transfer may takes place by states, e66 and e67, too.

5.2 Excitation energy transfer dynamics in PSII core complex(C2)



In the previous section, we present the efficient excitation energy transfer dynamics in a monomer of PSII core complex. In our work, we want to know the functional role of dimeric PSII core complex and to understand the energy transfer in the PSII core complex. In the subsection 5.1, we discover that the excitonic coupling between two CLA625s located in two adjacent CP47s is 5.14 cm^{-1} and lead to exciton states contributed by pigments located in two adjacent CP47s. We guess that excitation energy can flow between two adjacent CP47s by these exciton states. In this section, we propagate the energy transfer dynamics in PSII core complex to verify the inference from the subsection 5.1.

Four initial conditions are considered in this section. Figure 5.2 shows the excitation energy transfer dynamics with initial excitation at the CP47. Initial condition of Fig. 5.2a is equal population of exciton states contributed by pigments in the CP47 of M1 and initial condition of Fig. 5.2b is equal population of exciton states contributed by pigments in the CP47 of M2. In Fig. 5.2a, the population of the CP47 in the M1 decreases dramatically within 15 ps. At the same time, the population of the CP47 in the M2 increases and reach the maximum of 0.15 within about 10 ps. Also, the population of the RC in the M1 increases quickly within 3.5 ps and then excitation energy transfer to the CP43 in the M1 within 15 ps. At 300 ps, most of the exciton states become radical pairs. The population of radical pairs in the M2 increases, it implies that excitation energy can transfer to the RC in the M2 and then charge separation in the RC of M2. The total quantum yield of charge separation is 0.92. The same tendency of populations are showed in Fig. 5.2b. It indicates that excitation energy can flow between two monomers by passing through the CP47.

We also propagate the excitation energy transfer dynamics with initial excitation at the CP43. Initial condition of Fig. 5.3a is excitation at the CP43 of M1 and initial condition of Fig. 5.3b is excitation at the CP43 of M2. In Fig. 5.3a, excitation energy flow to the RC of the same monomer and then transfer to the CP47 of the same monomer. Then, the CP47 of the different monomer are excited. We can find that the population of RP1

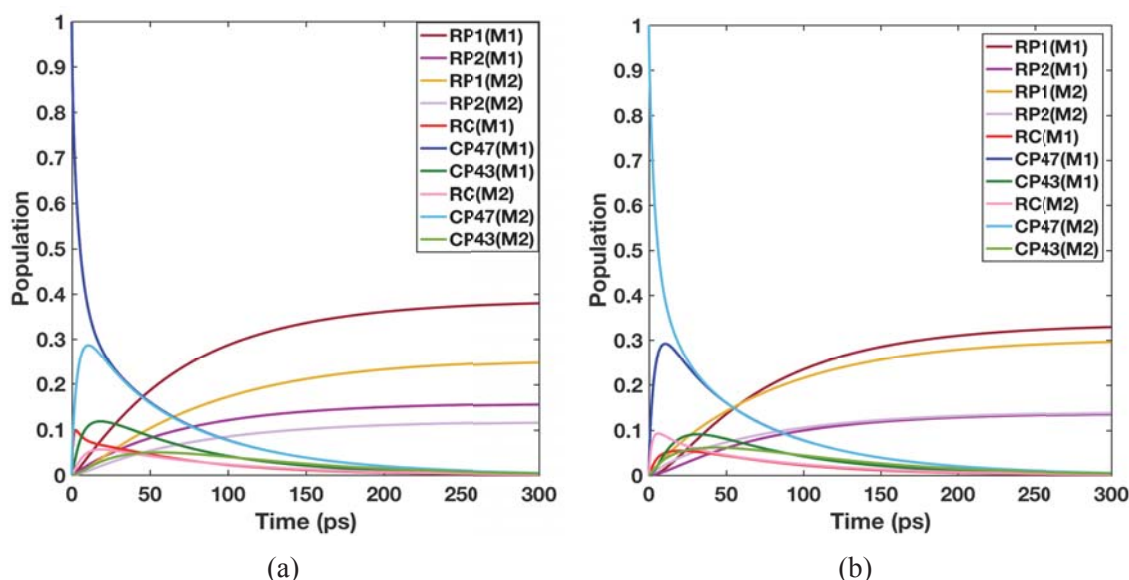


Figure 5.2: Excitation energy transfer for PSII core complex with initial excitation at the CP47. (a) Excitation energy transfer for PSII core complex with initial excitation at the CP47 of M1. The quantum yield of charge separation: RP1(M1) is 0.39; RP2(M1) is 0.16; RP1(M2) is 0.26; RP2(M2) is 0.12; (b) Excitation energy transfer for PSII core complex with initial excitation at the CP47 of the M2. The quantum yield of charge separation: RP1(M1) is 0.34; RP2(M1) is 0.14; RP1(M2) is 0.30; RP2(M2) is 0.14; Red line is the population of exciton states contributed by pigments in the RC of the M1. Blue line is the population of exciton states contributed by pigments in the CP47 of the M1. Green line is the population of exciton states contributed by pigments in in the CP43 of the M1. Pink line is the population of exciton states contributed by pigments in the RC of the M2. Cyan line is the population of exciton states contributed by pigments in the CP47 of the M2. Light green line is the population of exciton states contributed by pigments in in the CP43 of the M2. Brown line is the is the population of RP1 in the M1. Purple line is the population of RP2 in the M1. Yellow line is the population of RP1 in the M2. Light purple line is the population of RP2 in the M2.

in the M1 is dominant and is about 0.52 at 300 ps. Because the CP43 in the M1 is only adjacent to the RC in the M1, so most of the excitation energy may transfer to the RC in the M1 to charge separation. Energy transfer between these complex are within 30 ps. The population decay trace of the CP43 in Fig. 5.3a and Fig. 5.3b are slightly different. We also consider the site energy disorder in our model and the trace difference disappear.

In this section, we investigate the energy transfer dynamics in the PSII core complex. We discover the sub-ten picosecond dynamics between two CP47s. Also, excitation energy can transfer from one monomer to the other monomer to charge separation.

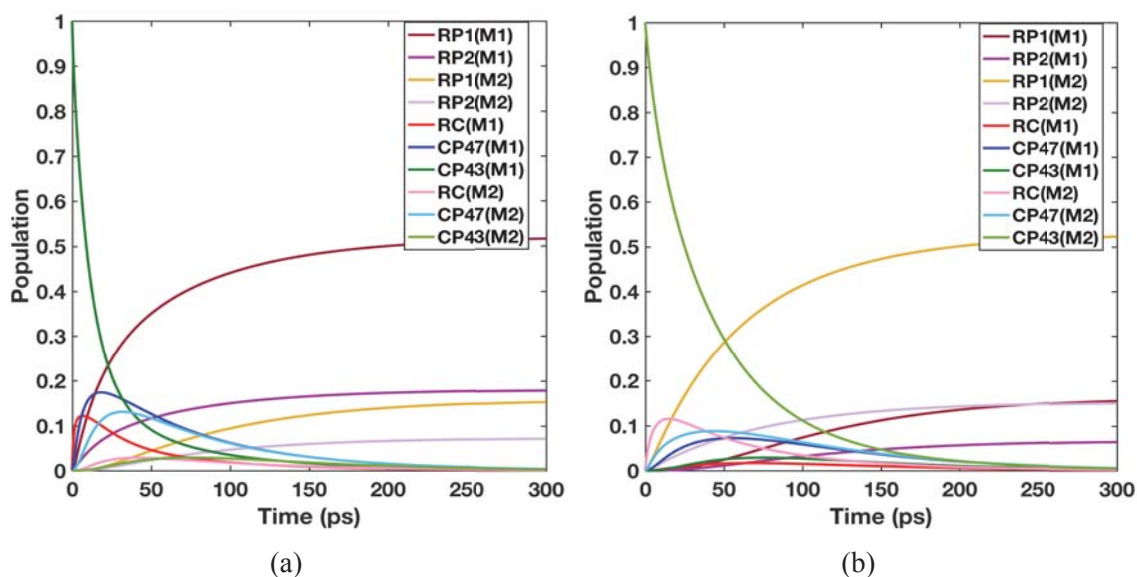


Figure 5.3: Excitation energy transfer for PSII core complex with initial excitation at the CP43. (a) Excitation energy transfer for PSII core complex with initial excitation at the CP43 of M1. The quantum yield of charge separation: RP1(M1) is 0.16; RP2(M1) is 0.07; RP1(M2) is 0.53; RP2(M2) is 0.15; (b) Excitation energy transfer for PSII core complex with initial excitation at the CP43 of the M2. The quantum yield of charge separation: RP1(M1) is 0.39; RP2(M1) is 0.16; RP1(M2) is 0.26; RP2(M2) is 0.12; Red line and pink line are the population of exciton states contributed by pigments in the RC of the M1 and the M2. Blue line and cyan line are the population of exciton states contributed by pigments in the CP47 of the M1 and the M2. Green line and light green line are the population of exciton states contributed by pigments in in the CP43 of the M1 and the M2. Brown line and yellow line are the is the population of RP1 in the M1 and the M2. Purple line and light purple line are the population of RP2 in the M1 and the M2.

5.3 Mutation and a closed RC for PSII core complex

In the previous section, we propagate excitation energy transfer dynamics based on our effective model. We find that excitation energy can be delivered throughout the whole PSII core complex. In particular, we find that energy transfer between two CP47s is very fast. How can excitation energy transfer so fast between two CP47s? In the subsection 5.1, we discover that the excitonic coupling of two CLA625s in two different CP47s are 5.14 cm^{-1} . Does the CLA625 play an important role in the energy transfer between two CP47s? In the following section, we remove two CLA625s in our model to investigate the contribution of CLA625 in the excitation energy transfer between monomers.

As we mentioned in the introduction, we want to know that why the PSII is in the form of dimer. As far as we know, PSII is an efficient engine for primary charge separation.

After the chlorophyll a in the RC transfer an electron to a plastoquinone, the RC is oxidized. The RC takes more than few nanoseconds to be reduced and open again. This time scale is larger than energy transfer in the PSII core complex. Excitation energy transfer to the RC, in which primary charge separation can't take place, can't be utilized efficiently and affect the quantum efficiency of charge separation. In our work, we define the RC, in which primary charge separation can't take place, as the closed RC. Therefore, effectively transferring excitation energy to the functional RC is also a factor affecting quantum yield. The dimeric structure results in two RCs are close to each other. Even if one of the RCs is closed, the other still have function and keep efficient charge transfer. Therefore, in this chapter, we also remove two formation rate of radical pairs in one of the RC to investigate the quantum yield of charge separation.

5.3.1 Excitation energy transfer for PSII core complex without CLA625s

In our mutant model, we remove site energies for two CLA625s and excitonic couplings between the CLA625 and the others pigments in our system Hamiltonian. In Fig. 5.4, we show the illustration of our mutant model and label the CLA625 as black color to represent the absence of these pigments.

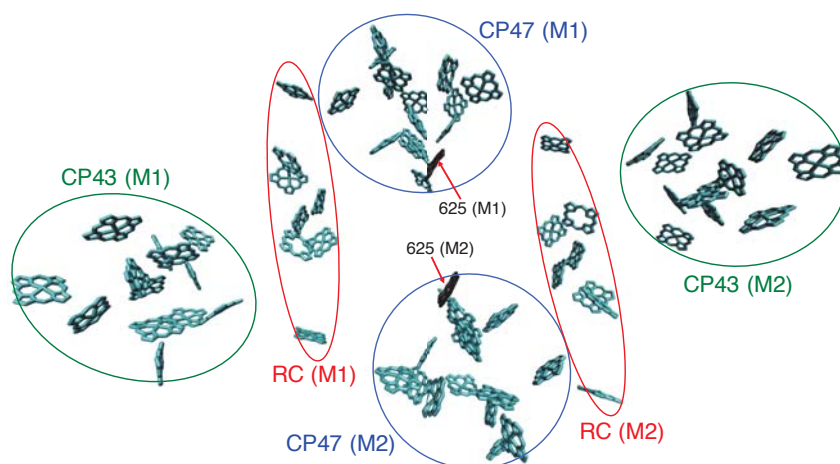


Figure 5.4: Illustration of PSII core complex without CLA625s. Chlorin rings in the crystal structure are shown. The blue ellipse represents the location of CP47 antenna complex. The red ellipse represents the location of RC. The green ellipse represents the location of CP43 antenna complex. CLA625s are labeled as black color to represent the absence of these pigments.

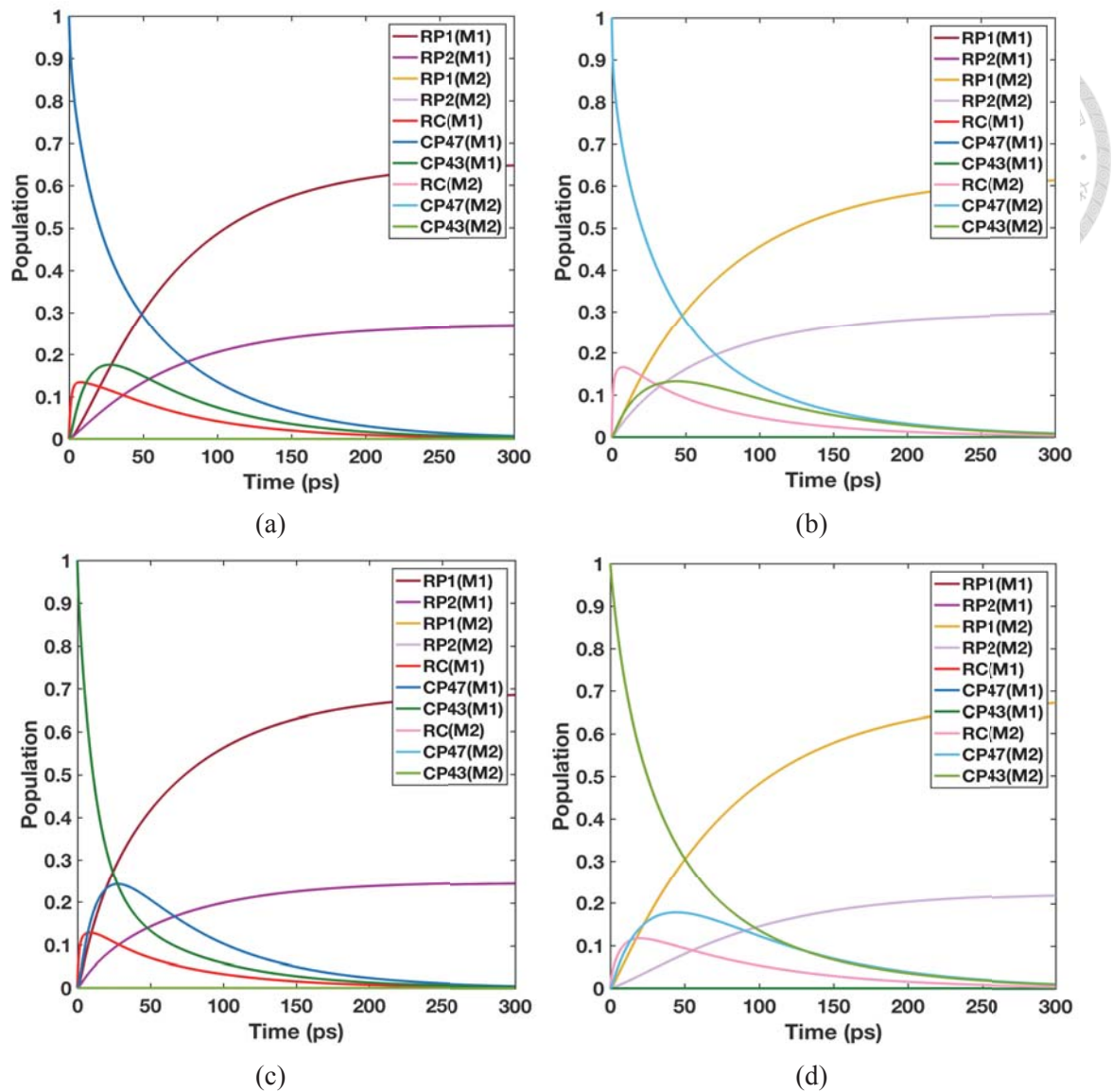


Figure 5.5: Excitation energy transfer for PSII core complex without CLA625s. (a) Excitation energy transfer with initial excitation at the CP47 of M1. The quantum yield of charge separation: RP1(M1) is 0.66; RP2(M1) is 0.27. (b) Excitation energy transfer with initial excitation at the CP47 of the M2. The quantum yield of charge separation: RP1(M2) is 0.63; RP2(M2) is 0.30. (c) Excitation energy transfer with initial excitation at the CP43 of the M1. The quantum yield of charge separation: RP1(M1) is 0.69; RP2(M1) is 0.25. (d) Excitation energy transfer with initial excitation at the CP43 of the M2. The quantum yield of charge separation: RP1(M2) is 0.69; RP2(M2) is 0.23. Red line and pink line are the population of exciton states contributed by pigments in the RC of the M1 and the M2. Blue line and cyan line are the population of exciton states contributed by pigments in the CP47 of the M1 and the M2. Green line and light green line are the population of exciton states contributed by pigments in the CP43 of the M1 and the M2. Brown line and yellow line are the population of RP1 in the M1 and the M2. Purple line and light purple line are the population of RP2 in the M1 and the M2.

Figure 5.5a is initial excitation at the CP47 of the M1. We can discover that the population of antenna complexes, RC, and radical pairs in the M2 is always zero. That is, excitation energy can't flow to the other monomer. It leads to the trend of populations is similar to the dynamics of a monomer (Fig. 4.3). The total quantum yield of charge separation is 0.93. It keeps the high efficiency of charge separation. The similar trend are discovered with the initial excitation at the CP47 in the M2 in Fig. 5.5b. Excitation energy flowing to the CP43 in the M2 is slightly slower. The trace difference may disappear after considering the site energy disorder. Figure 5.5c and Fig. 5.5c are initial excitation at the CP43 in the M1 and M2, respectively. The excitation energy can flow within the monomer which is excited, but the quantum yield is still high enough.

By the mutant model, we prove that CLA625s play an important role in the energy transfer between two CP47s. Although *Chlz_{D1}* in the RC and CLA616 in the CP47 between different monomers are close to each other in Fig. 5.6, we didn't find the energy transfer between the RC and the CP47. Excitation energy transfer between two monomers occurs only in the present of CLA625s. Therefore, CLA625s are an energy bridge that allows energy to flow between monomers.

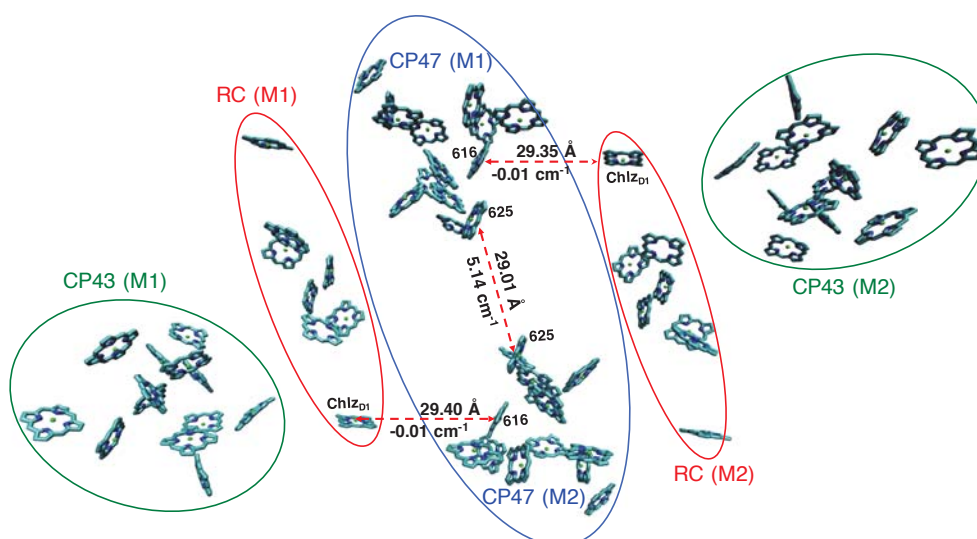
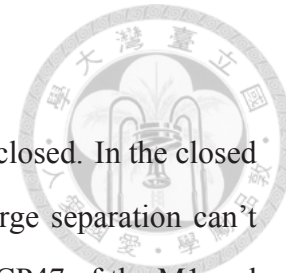


Figure 5.6: Illustration of CP47s as an energy regulator. Chlorin rings in the crystal structure are shown. The blue ellipse represents two CP47s are an energy regulator. The red ellipses represent the location of RCs. The green ellipses represent the location of CP43 antenna complex. The distance and the excitonic coupling between each pair are shown above and below the arrow.

5.3.2 Excitation energy transfer for PSII core complex with a closed RC



In this section, we mimic the dynamics when one of the RCs is closed. In the closed RC, excitation energy can flow into and flow out the RC, but charge separation can't take place in the closed RC. In Fig. 5.7a, initial excitation is in the CP47 of the M1 and also the RC in the M1 is closed. Because the population of exciton states is converted to the population of radical pairs until 1500 ps, we propagate the dynamics to 1500 ps and also define the quantum yield as the population of radical pairs at 1500 ps. It is obvious that the population trend of the CP47 in the M1 is composed of two apparent decay times. ($P_{CP47(M1)}(t) = 0.59e^{-\frac{t}{6.03}} + 0.28e^{-\frac{t}{181.39}}$) The fast 6.03 ps decay time is caused by very fast excitation energy transfer to the other CP47 and then to the CP43 and the RC in the M1. The slow decay after 30 ps is similar to the decay trend for the CP47 in the M2. The time scale for slow decay time are close to the formation lifetimes for radical pairs. Because the rate constants for two radical pairs formation in the rate constant matrix is less than 5 ps, the formation lifetimes for radical pairs in Fig. 5.7a is contributed by energy migration time to reach Chl_{D1} or P_{D1} . Therefore, the slow decay time may be the migration time to reach Chl_{D1} or P_{D1} . The total quantum yield for this system is 0.80, which is lower than previous conditions. The same trend is investigated in the initial excitation of CP47 in the M2 in Fig. 5.7b. The total quantum yield is 0.83.

In Fig. 5.7c, initial excitation is in the CP43 of the M1 and also the RC in the M1 is closed. The population trend of the CP43 is composed of two apparent lifetimes, too. ($P_{CP43(M1)}(t) = 0.67e^{-\frac{t}{11.19}} + 0.28e^{-\frac{t}{176.93}}$) The fast apparent lifetime leads to excitation energy delocalized in two CP47s, the CP43 in the M1, and the RC in the M1. The population of them are around 0.15 to 0.23 at 50 ps. Then, all of them decay slowly to transfer energy to RC of M2 for charge separation. The total quantum yield is 0.78 in Fig. 5.7c and 5.7d.

According to the dynamics simulated in our work, although one of the RCs is closed, the quantum yield can be kept above 0.75 due to the energy transfer smoothly between two monomers. Also, excitation energy can delocalize in the PSII core complex within

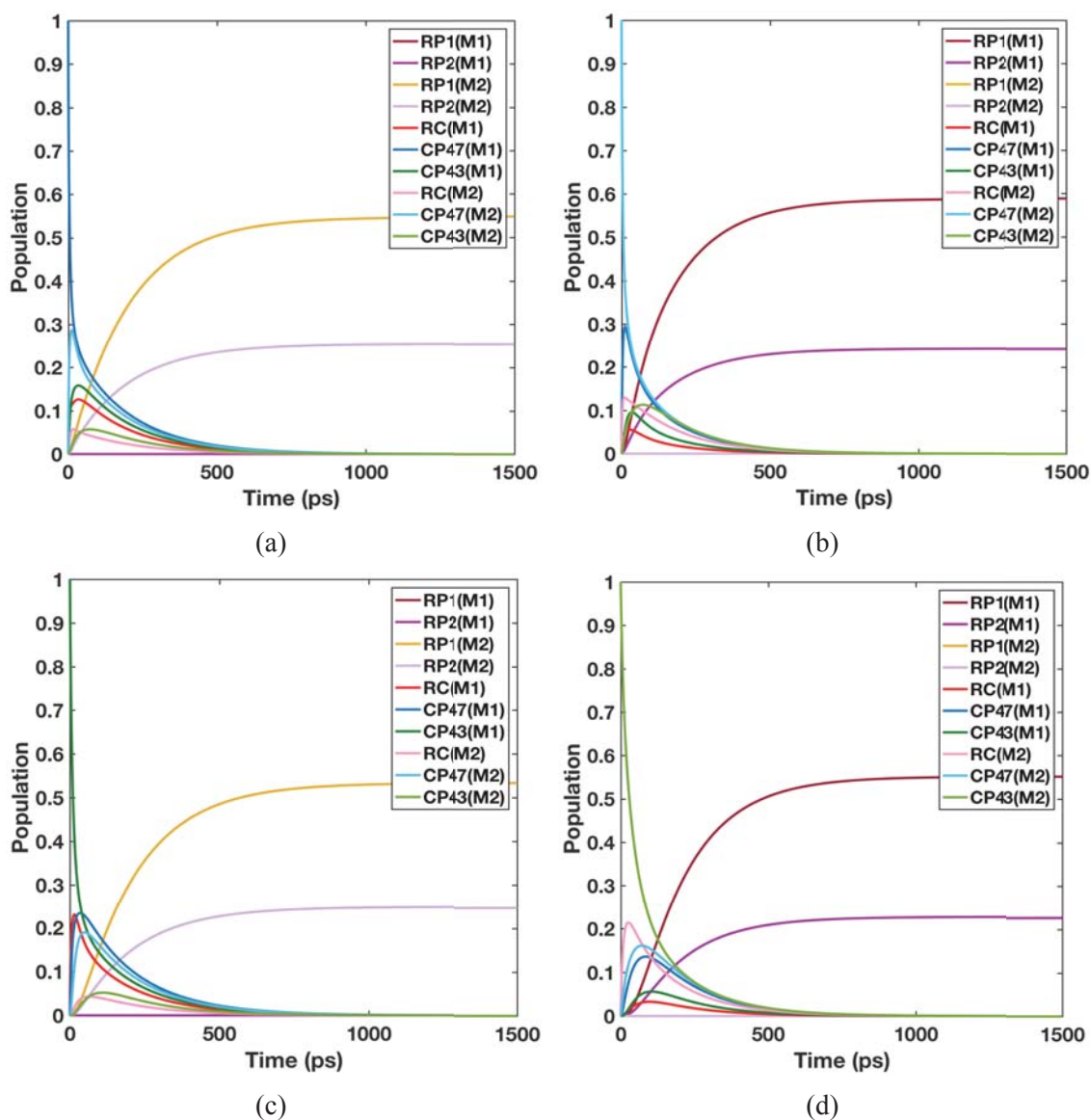


Figure 5.7: Excitation energy transfer for PSII core complex with a closed RC. (a) Excitation energy transfer with initial excitation at the CP47 of M1 and a closed RC in the M1. The quantum yield of charge separation: RP1(M2) is 0.55; RP2(M2) is 0.25. (b) Excitation energy transfer with initial excitation at the CP47 of the M2 and a closed RC in the M2. The quantum yield of charge separation: RP1(M1) is 0.59; RP2(M1) is 0.24. (c) Excitation energy transfer with initial excitation at the CP43 of the M1 and a closed RC in the M1. The quantum yield of charge separation: RP1(M2) is 0.53; RP2(M2) is 0.25. (d) Excitation energy transfer with initial excitation at the CP43 of the M2 and a closed RC in the M2. The quantum yield of charge separation: RP1(M1) is 0.55; RP2(M1) is 0.23. Red line and pink line are the population of exciton states contributed by pigments in the RC of the M1 and the M2. Blue line and cyan line are the population of exciton states contributed by pigments in the CP47 of the M1 and the M2. Green line and light green line are the population of exciton states contributed by pigments in the CP43 of the M1 and the M2. Brown line and yellow line are the population of RP1 in the M1 and the M2. Purple line and light purple line are the population of RP2 in the M1 and the M2.

about dozens of picoseconds. However, the quantum yield is slightly lower than previous simulations because energy takes more time to go to the farther RC.



5.3.3 Excitation energy transfer for mutant PSII core complex with a closed RC

In the previous section, we discover excitation energy transfer between two monomers is a key factor for the efficient quantum yield when one of the RC is closed. What if excitation energy can't transfer from one monomer to the other monomers when one of the RCs is closed? How much will the quantum yield drop when one of the RC is closed and excitation energy can't transfer between two monomer? In this section, we initially excite two CP47s in our mutant model, which is lack of CLA625s, and the dynamics is showed in Fig. 5.8.

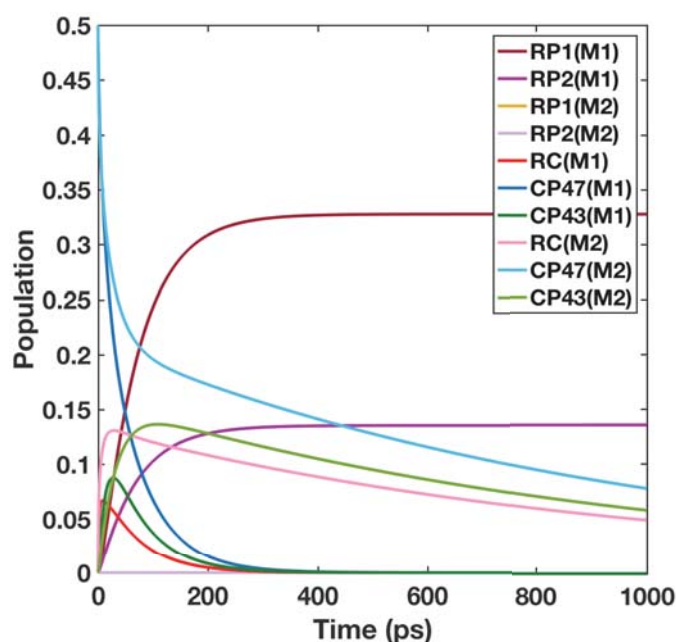


Figure 5.8: Excitation energy transfer for mutant PSII core complex with a closed RC. Initial condition is equal population for exciton states contributed by pigments in two CP47s. The RC in the M2 is closed. The quantum yield of charge separation: RP1(M1) is 0.33; RP2(M1) is 0.14. Red line and pink line are the population of exciton states contributed by pigments in the RC of the M1 and the M2. Blue line and cyan line are the population of exciton states contributed by pigments in the CP47 of the M1 and the M2. Green line and light green line are the population of exciton states contributed by pigments in the CP43 of the M1 and the M2. Brown line and yellow line are the population of RP1 in the M1 and the M2. Purple line and light purple line are the population of RP2 in the M1 and the M2.

In Fig. 5.8, because the RC in the M1 is opened, excitation energy transfer in the M1 are similar to the case of monomer in our model. However, the dynamics of excitation energy transfer in the M2 are really different. The decay trend for the population of the CP47 in the M2 is composed of two exponential decay. ($P_{CP47(M2)}(t) = 0.21e^{-\frac{t}{22.40}} + 0.21e^{-\frac{t}{991.08}}$) The 22 ps decay time is contributed by energy transfer from CP47 in the M2 to the CP43 and the RC in the M2. The 991 ps lifetime is close to the fluorescence lifetime (1 ns), so excitation energy can't reach the functional RC and is released by fluorescence.

According to above results, two CP47s just like an energy regulator to regulate excitation energy to achieve efficient quantum yield of charge separation. In addition, two CLA625 are the only channel for energy transfer between two monomers, so the PSII core complex without CLA625s may have lower quantum yield of charge separation. Furthermore, we discover that there are four β -carotenes in the CP47 and three of them are close to CLA625 in the Fig 5.9. At the high light condition, excitation energy at the CLA625 may transfer energy to β -carotenes to quench excitation energy for photo-protection [48].

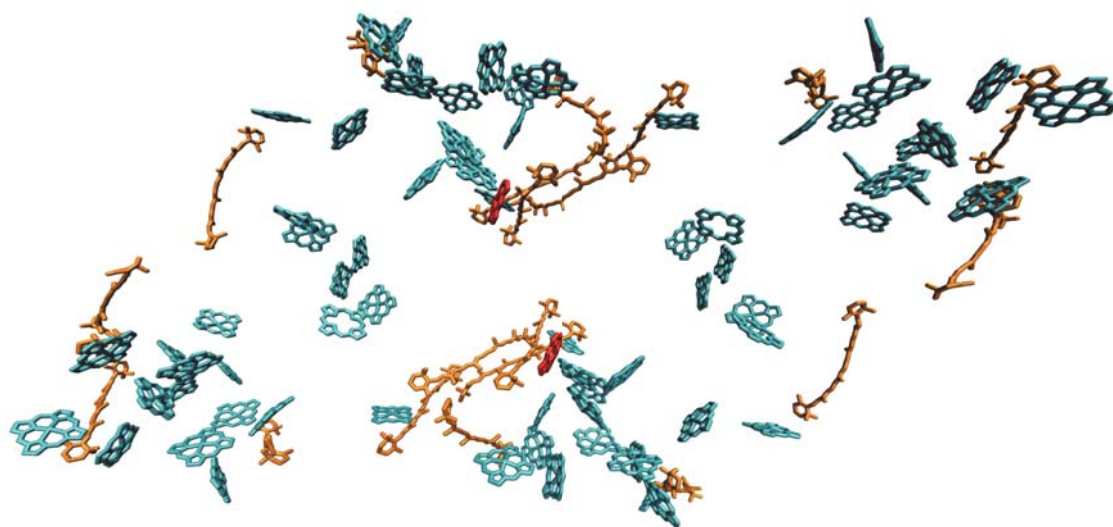


Figure 5.9: Illustration of PSII core complex with β -carotenes. Chlorin rings in the crystal structure represent the chlorophyll a and the pheophytin, which is lack of a magnesium in the center of the ring. β -carotenes are shown in orange. CLA625s are shown in red.



Chapter 6

Conclusion

In this work, we construct a structure-based effective model for PSII core complex. Average site energies based on MD simulation from Huang's group and excitonic couplings based on crystal structure are utilized in the system Hamiltonian. To correctly simulate excitation energy transfer dynamics, we apply the harmonic quantum correction to the energy gap auto-correlation function from trajectories of site energy to obtain the quantum time correlation function. Also, we calculate the population transfer rate between exciton states based on modified Redfield theory and propagate dynamics by the master equation.

Our model describes the absorption spectrum of the CP47, the CP43 and the RC at 297 K as well as the full excitation energy transfer dynamics among the 74 pigments in the PSII core complex. We discover that the higher-energy sites, such as Phe_{D1} , CLA613, and CLA638, and the lower-energy sites, Chl_{D1} , CLA612, and CLA636, are adjacent in the RC, the CP47, and the CP43, respectively. It leads to higher-energy exciton states and lower-energy exciton states are contributed by same sites, so fast excitation energy transfer between these exciton states takes place.

In the monomer of PSII core complex, we can find that energy transfer between two antenna complexes takes place through the RC. It can be explained by the five exciton states contributed by pigments between antenna complexes, CP47 and CP43, and the RC due to excitonic couplings of pigments between antenna complexes and the RC, such as $Chl_{z_{D2}}$ and CLA612, and Phe_{D1} and CLA635. That is to say, excitation energy transfer

between antenna complexes and the RC is reversible. Also, energy can flow into and then flow out the RC.

In the PSII core complex, we discover that excitation energy transfer between monomers is governed by energy transfer between two CP47s. Although *Chlz_{D1}* in the RC and CLA616 in the CP47 between different monomers are close to each other, we didn't find the energy transfer between the RC and the CP47. We also discover that among the distance of pigments between two monomers, the distance of two CLA625s in different CP47s is shortest. Due to the shortest distance, they have the strongest excitonic coupling. Therefore, we prove that two CLA625s in the CP47 is an energy bridge to allow excitation energy flow between monomers by our mutant model. After removing two CLA625s in the system Hamiltonian, excitation energy can't transfer between two monomers.

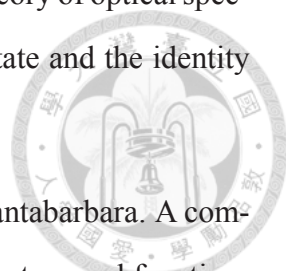
In addition, we close one of the RCs in the PSII core complex and find that the quantum yield of charge separation drops from about 0.9 to about 0.80. Excitation energy in the monomer with closed RC may transfer to the other RC to charge separation. The reason why the quantum yield drop is that the energy migration time from one monomer to the other monomer is larger than the energy migration time within a monomer. Also, in the PSII core complex without two CLA625, if one of the RCs is closed, the quantum yield of charge separation is less than 0.5. This result emphasizes the importance of energy transfer between monomers.

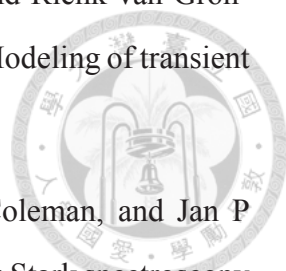
Last but not least, we propose a reason why PSII core complex form in a dimer. In the dimeric PSII core complex, two CP47s are the nearest neighbor and become an energy regulator. They effectively regulate energy to transfer to the functional RC. Our model shows that a first principle method based on MD simulations and quantum chemistry calculations can provide a new insight to understand the function-structure relationship for a PSII core complex and is effectively utilized to investigate the light harvesting in complicate photosynthetic complexes.

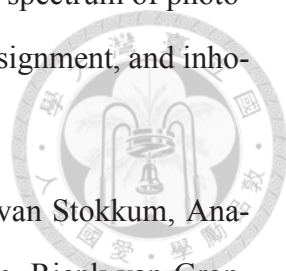


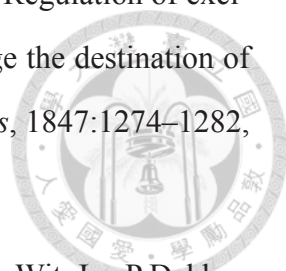
Bibliography

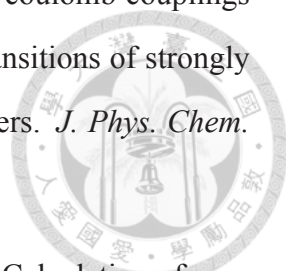
- [1] Govindjee. Adventures with cyanobacteria: a personal perspective. *Front. Plant Sci.*, 2:1–17, 2011.
- [2] Robert E. Blankenship. *Molecular mechanisms of photosynthesis*. Blackwell Science Ltd, Oxford, UK, 2008.
- [3] Jon Nield and James Barber. Refinement of the structural model for the Photosystem II supercomplex of higher plants. *Biochim. Biophys. Acta - Bioenerg.*, 1757:353–361, 2006.
- [4] Xuepeng Wei, Xiaodong Su, Peng Cao, Xiuying Liu, Wenrui Chang, Mei Li, Xinzheng Zhang, and Zhenfeng Liu. Structure of spinach photosystem II-LHCII supercomplex at 3.2 Å resolution. *Nature*, 534:69–74, 2016.
- [5] X. Pan, Z. Liu, M. Li, and W. Chang. Architecture and function of plant light-harvesting complexes II. *Curr. Opin. Struct. Biol.*, 23:515–525, 2013.
- [6] Doran I.G. Bennett, Kapil Amarnath, and Graham R. Fleming. A structure-based model of energy transfer reveals the principles of light harvesting in photosystem II supercomplexes. *J. Am. Chem. Soc.*, 135:9164–9173, 2013.
- [7] S Vasil’ev, P Orth, A Zouni, T G Owens, and D Bruce. Excited-state dynamics in photosystem II: insights from the x-ray crystal structure. *Proc Natl Acad Sci U S A*, 98:8602–8607, 2001.

- 
- [8] Grzegorz Raszewski, Wolfram Saenger, and Thomas Renger. Theory of optical spectra of photosystem II reaction centers: Location of the triplet state and the identity of the primary electron donor. *Biophys. J.*, 88:986–998, 2005.
- [9] Stefano Caffarri, Tania Tibiletti, Robert Jennings, and Stefano Santabarbara. A comparison between plant Photosystem I and Photosystem II architecture and functioning. *Curr. Protein Pept. Sci.*, 15:296–331, 2014.
- [10] Allison M L van de Meene, Martin F Hohmann-Marriott, Wim F J Vermaas, and Robert W Roberson. The three-dimensional structure of the cyanobacterium *Synechocystis* sp. PCC 6803. *Arch. Microbiol.*, 184:259–270, 2006.
- [11] Jacqueline Olive, Ghada Ajlani, Chantal Astier, Michel Recouvreur, and Claudie Vernotte. Ultrastructure and light adaptation of phycobilisome mutants of *Synechocystis* PCC 6803. *Biochim. Biophys. Acta (BBA)-Bioenergetics*, 1319:275–282, 1997.
- [12] Tihana Mirkovic, Evgeny E. Ostroumov, Jessica M. Anna, Rienk Van Grondelle, Govindjee, and Gregory D. Scholes. Light absorption and energy transfer in the antenna complexes of photosynthetic organisms. *Chem. Rev.*, 117:249–293, 2017.
- [13] Yasufumi Umena, Keisuke Kawakami, Jian Ren Shen, and Nobuo Kamiya. Crystal structure of oxygen-evolving photosystem II at a resolution of 1.9Å. *Nature*, 473:55–60, 2011.
- [14] Lu Zhang, Daniel Adriano Silva, Houdao Zhang, Alexander Yue, Yijing Yan, and Xuhui Huang. Dynamic protein conformations preferentially drive energy transfer along the active chain of the photosystem II reaction centre. *Nat. Commun.*, 5:1–9, 2014.
- [15] Elisabet Romero, Ivo H M Van Stokkum, Vladimir I. Novoderezhkin, Jan P. Dekker, and Rienk Van Grondelle. Two different charge separation pathways in photosystem II. *Biochemistry*, 49:4300–4307, 2010.

- 
- [16] Vladimir I Novoderezhkin, Elisabet Romero, Jan P Dekker, and Rienk van Grondelle. Multiple charge-separation pathways in Photosystem II: Modeling of transient absorption kinetics. *ChemPhysChem*, 12:681–688, 2011.
- [17] Elisabet Romero, Bruce A Diner, Peter J Nixon, William J Coleman, and Jan P Dekker. Mixed exciton –charge-transfer states in photosystem II : Stark spectroscopy on site-directed mutants. *Biophys. J.*, 103:185–194, 2012.
- [18] Bart Van Oort, Marieke Alberts, Silvia De Bianchi, Luca Dall’Osto, Roberto Bassi, Gediminas Trinkunas, Roberta Croce, and Herbert Van Amerongen. Effect of antenna-depletion in photosystem II on excitation energy transfer in *Arabidopsis thaliana*. *Biophys. J.*, 98:922–931, 2010.
- [19] Emilie Wientjes, Herbert van Amerongen, and Roberta Croce. Quantum yield of charge separation and fluorescence in photosystem II of green plants. *J. Phys. Chem. B*, 117:11200–11208, 2013.
- [20] Nathan Nelson and Wolfgang Junge. Structure and energy transfer in photosystems of oxygenic photosynthesis. *Annu. Rev. Biochem.*, 84(1):659–683, 2015.
- [21] William W. Adams, Barbara Demmig-Adams, Klaus Winter, and Ulrich Schreiber. The ratio of variable to maximum chlorophyll fluorescence from photosystem II, measured in leaves at ambient temperature and at 77K, as an indicator of the photon yield of photosynthesis. *Planta*, 180:166–174, 1990.
- [22] Vladimir I. Novoderezhkin, Elena G. Andrizhiyevskaya, Jan P. Dekker, and Rienk Van Grondelle. Pathways and timescales of primary charge separation in the photosystem II reaction center as revealed by a simultaneous fit of time-resolved fluorescence and transient absorption. *Biophys. J.*, 89:1464–1481, 2005.
- [23] Yutaka Shibata, Shunsuke Nishi, Keisuke Kawakami, Jian Ren Shen, and Thomas Renger. Photosystem II does not possess a simple excitation energy funnel: Time-resolved fluorescence spectroscopy meets theory. *J. Am. Chem. Soc.*, 135:6903–6914, 2013.

- 
- [24] L. Konermann and A. R. Holzwarth. Analysis of the absorption spectrum of photosystem II reaction centers: temperature dependence, pigment assignment, and inhomogeneous broadening. *Biochemistry*, 35:829–42, 1996.
- [25] Raoul N Frese, Marta Germano, Frank L de Weerd, Ivo H M van Stokkum, Anatoli Ya Shkuropatov, Vladimir a Shuvalov, Hans J van Gorkom, Rienk van Grondelle, and Jan P Dekker. Electric field effects on the chlorophylls, pheophytins, and beta-carotenes in the reaction center of photosystem II. *Biochemistry*, 42:9205–9213, 2003.
- [26] ML Groot, JP Dekker, R van Grondelle, FTH Den Hartog, and S Völker. Energy transfer and trapping in isolated photosystem II reaction centers of green plants at low temperature. A study by spectral hole burning. *J Phys Chem*, 3654:11488–11495, 1996.
- [27] Gunther H Schatz, Helmut Brock, and Alfred R Holzwarth. Picosecond kinetics of fluorescence and absorbance changes in photosystem II particles excited at low photon density. *Proc. Natl. Acad. Sci. U. S. A.*, 84:8414–8, 1987.
- [28] Günther H Schatz, Helmut Brock, and Alfred R Holzwarth. Kinetic and energetic model for the primary processes in Photosystem II. *Biophys. J.*, 54:397–405, sep 1988.
- [29] Jan P. Dekker and Rienk Van Grondelle. Primary charge separation in photosystem ii. *Photosynthesis Research*, 63:195–208, 2000.
- [30] Yusuke Yoneda, Tetsuro Katayama, Yutaka Nagasawa, Hiroshi Miyasaka, and Yasufumi Umena. Dynamics of excitation energy transfer between the subunits of Photosystem II dimer. *J. Am. Chem. Soc.*, 138:11599–11605, 2016.
- [31] Ahmed Mohamed, Ryo Nagao, Takumi Noguchi, Hiroshi Fukumura, and Yutaka Shibata. Structure-based modeling of fluorescence kinetics of photosystem II: relation between its dimeric form and photoregulation. *J. Phys. Chem. B*, 120:365–376, 2016.

- 
- [32] Makio Yokono, Ryo Nagao, Tatsuya Tomo, and Seiji Akimoto. Regulation of excitation energy transfer in diatom PSII dimer: How does it change the destination of excitation energy? *Biochim. Biophys. Acta (BBA)-Bioenergetics*, 1847:1274–1282, 2015.
- [33] Koen Broess, Gediminas Trinkunas, Chantal D. Van Der Weij-De Wit, Jan P Dekker, Arie Van Hoek, and Herbert Van Amerongen. Excitation energy transfer and charge separation in photosystem II membranes revisited. *Biophys. J.*, 91:3776–3786, 2006.
- [34] Thomas Renger and Frank Müh. Understanding photosynthetic light-harvesting: a bottom up theoretical approach. *Phys. Chem. Chem. Phys.*, 15:3348–3371, 2013.
- [35] Thomas Renger, Volkhard May, and Oliver Ku. Ultrafast excitation energy transfer dynamics in photosynthetic pigment protein complexes. *Phys. Rep.*, 343:137–254, 2001.
- [36] A Davydov. *Theory of molecular excitons*. Springer, 2013.
- [37] Mino Yang and Graham R Fleming. Influence of phonons on exciton transfer dynamics: comparison of the Redfield, Forster, and modified Redfield equations. *Chem. Phys.*, 275:355–372, 2002.
- [38] M. E. Madjet, A. Abdurahman, and T. Renger. Intermolecular coulomb couplings from ab initio electrostatic potentials: Application to optical transitions of strongly coupled pigments in photosynthetic antennae and reaction centers. *J. Phys. Chem. B*, 110:17268–17281, 2006.
- [39] Julia Adolphs, Frank Müh, Mohamed El Amine Madjet, and Thomas Renger. Calculation of pigment transition energies in the FMO protein: From simplicity to complexity and back. *Photosynth. Res.*, 95:197–209, 2008.
- [40] J Adolphs, F Muh, Me-a Madjet, Marcel Schmidt am Busch, and Thomas Renger. Structure-based calculation of optical spectra of Photosystem I suggest an asymmetric light-harvesting process. *J. Am. Chem. Soc.*, 132:3331–3343, 2010.

- 
- [41] M. E. Madjet, A. Abdurahman, and T. Renger. Intermolecular coulomb couplings from ab initio electrostatic potentials: Application to optical transitions of strongly coupled pigments in photosynthetic antennae and reaction centers. *J. Phys. Chem. B*, 110:17268–17281, 2006.
- [42] Brent P Krueger, Gregory D Scholes, and Graham R Fleming. Calculation of couplings and energy-transfer pathways between the pigments of LH2 by the ab initio transition density cube method. *J. Phys. Chem. B*, 102:5378–5386, 1998.
- [43] Thomas Renger, Mohamed El-Amine Madjet, Marcel Schmidt Am Busch, Julian Adolphs, and Frank Müh. Structure-based modeling of energy transfer in photosynthesis. *Photosynth. Res.*, 116:367–388, 2013.
- [44] Gregory D Scholes, Carles Curutchet, Benedetta Mennucci, Roberto Cammi, and Jacopo Tomasi. How solvent controls electronic energy transfer and light harvesting. *J. Phys. Chem. B*, 111:6978–6982, 2007.
- [45] David Chandler. *Introduction to modern statistical mechanics*. New York, 1987.
- [46] Stéphanie Valleau, Alexander Eisfeld, and Alán Aspuru-Guzik. On the alternatives for bath correlators and spectral densities from mixed quantum-classical simulations. *J. Chem. Phys.*, 137, 2012.
- [47] Vladimir I Novoderezhkin, Danielis Rutkauskas, and Rienk van Grondelle. Dynamics of the emission spectrum of a single LH2 complex: interplay of slow and fast nuclear motions. *Biophys. J.*, 90:2890–2902, 2006.
- [48] Grzegorz Raszewski and Thomas Renger. Light harvesting in photosystem II core complexes is limited by the transfer to the trap: Can the core complex turn into a photoprotective mode? *J. Am. Chem. Soc.*, 130:4431–4446, 2008.